Sum Frequency Generation Vibrational Spectroscopy Studies of Adsorbates on Pt(111): Studies of CO at High Pressures and Temperatures, Coadsorbed with Olefins and its Role as a Poison in Ethylene Hydrogenation

by

Kyle Yi Kung

B.S. (Colorado State University) 1996

A dissertation submitted in partial satisfaction of the

requirements for the degree of

Doctor of Philosophy

in

Chemistry

in the

GRADUATE DIVISION

of the

UNIVERSITY OF CALIFORNIA, BERKELEY

Committee in Charge:

Professor Gabor A. Somorjai, Chair
Professor Yuen R. Shen
Professor C. Bradley Moore

Fall 2000

Acknowledgments

First, I would like to extend my sincere gratitude to my advisor Professor Gabor A. Somorjai for the opportunity to conduct research in his group. His scientific intuition and enthusiasm have guided me through my research. His insights on science and in life are those I will always carry with me.

Professor Y.R. Shen served as my coadvisor and I extremely grateful for his wisdom and patience. Through him, I have learned to appreciate the intricacies of nature.

Graduate school at Berkeley has served as forum for learning to conduct world class research as well as for personal development. To which I would like to thank my mentors of Enrico Magni, Howard Fairbrother, Paul Cremer, and Peilin Chen. My detailed knowledge of UHV, surface science, catalysis and nonlinear laser spectroscopy results from their patience. I cannot thank them enough for their friendship. I am especially thankful to Enrico for teaching me about the essence of working for one's self.

I thank John Jensen and Joel Roberts for teaching me UHV as well as allowing me to "borrow" their equipment.

I thank Rodney Chin, Steve Baldelli and Xingcai Su for teaching me SFG. I am extremely thankful to Xing Wei for always being there to help with my understanding of SFG and nonlinear optics.

I thank Keith Rider for our strange conversation topics and teaching me how to fly fish. It was really nice to talk to another person about a variety of subjects and be emotionally detached about them.

I thank my fellow group members of Yong Chen, Andre Ramos, Saskia Hoffer, Leo Lianos, Edmar Soares, and Dina Zhang, for their discussions, assistance and friendship.

I like to also thank Frank Wei, for his friendship and for working with me as an undergraduate. His work ethic and integrity are traits I admire. I wish him the best of luck as he starts his graduate career at MIT.

I am grateful to my classmates Sid Patil, Simon Liu, Andre Miller and Melissa Sander, for their friendship. Their friendship from the beginning of graduate school made this experience enjoyable.

I thank Eric Granlund, James Wu, and Henry Chan for all of their assistance to my research. It would have been quite unimaginable without them.

I like to thank Professor Nancy Levinger at Colorado State University for teaching me the tools to be successful in graduate school and in life. Without her support and guidance, I would not have made it this far.

On a personal note, I like to thank my roommates Joel and Virginia Loo for making home life truly enjoyable. I am extremely indebted to Joel for sharing his outlook on life and graduate school. I thank Virginia for her extraordinary kindness and her baking. She makes the best cookies I have ever had. Joel and Virginia are remarkable for putting up with my curiosity and questioning. I like

to also thank my friends Vince Cambra, Troy Horton, Dave Dickinson, Martin Tsai, Jeff and Francesca Clubs for their support, long friendship, and their visits to the bay area. I would also like to thank George Chen for showing me Taiwan, teaching me about people and to not be afraid to ask for big things. I like to thank Andre, Jamie Lin and their families for welcoming me to their home and taking care of me in Brazil.

To my mother, Jenny, father, James, sister, Betty and brother, Ean thanks for your love and support and believing in me.

Table of Contents

Abstract

Sum Frequency Generation Vibrational Spectroscopy Studies of Adsorbates on Pt(111): Studies of CO at High Pressures and Temperatures, Coadsorbed with Olefins and its Role as a Poison in Ethylene Hydrogenation

by

Kyle Yi Kung

Doctor of Philosophy in Chemistry

University of California, Berkeley

Professor Gabor A. Somorjai, Chair

High pressure high temperature CO adsorption and coadsorption with ethylene and propylene on Pt(111) was monitored in situ with infrared-visible sum frequency generation (SFG). At high pressures and high temperatures, CO dissociates on a Pt(111) surface to form carbon. At 400 torr CO pressure and 673K, CO modifies the Pt(111) surface through a carbonyl intermediate, and dissociates to leave carbon on the surface. SFG was used to follow the CO peak evolution from monolayer adsorption in ultra high vacuum (UHV) to 400 torr CO pressure. At this high pressure, a temperature dependence study from room temperature to 823K was carried out. Auger electron spectroscopy was used to identify carbon on the surface

CO coadsorption with ethylene and CO coadsorption with propylene studies were carried out with 2-IR 1-visible SFG. With this setup, two spectral ranges covering the C-H stretch range and the CO stretch range can be monitored simultaneously. The coadsorption study with ethylene reveals that after 5L ethylene exposure on a Pt(111) surface to form ethylidyne , CO at high pressures cannot completely displace the ethylidyne from the surface. Instead, CO first adsorbs on defect sites at low pressures and then competes with ethylidyne for terrace sites at high pressures. Propylene coadsorption with CO at similar conditions shows that propylidyne undergoes conformation changes with increased CO pressure and at 1 torr, is absent from the Pt(111) surface.

Experiments on CO poisoning of ethylene hydrogenation was carried by 2-IR 1-visible SFG. At 1 torr CO,10 torr ethylene and 100 torr hydrogen, CO was found to block active sites necessary for ethylene hydrogenation, Above 425K, CO desorbs from the surface to allow ethylene hydrogenation to occur. The gas phase species were monitored by gas chromatography.

Chapter 1

Introduction

The advent of ultra high vacuum (UHV) provided the foundation for building our knowledge of surface science and catalysis of transition metals. A wealth of information on how and where molecules adsorb on these surfaces came as a result. While we have learned great insights to these model systems, it often falls short in its relevance to real world systems. The assumption that model system behavior under low pressures is directly transferable to its high-pressure counterpart does not often fall true. Under high pressures, adsorbates can form structures not see previously in low pressures and relevant long lived surface reaction intermediate species can be observed. While UHV gives us the starting point of a clean and well ordered surface and its various electron based surface analytical tools of Auger Electron Spectroscopy (AES), Low Energy Electron Diffraction (LEED) and High Resolution Electron Energy Loss Spectroscopy (HREELS) provide a wealth of information on surface structure and composition, they can not bridge the pressure gap when systems move toward ambient conditions.[1] The use of light based techniques like Infrared-Visible Sum Frequency Generation (SFG) and Second Harmonic Generation (SHG), which are inherently surface sensitive, allows for study of any surface that is accessible by

light. With SFG, surface reaction intermediates can be correlated with reaction kinetics as determined by gas chromatography.[2]

Infrared-Visible Sum Frequency Generation has been developed into a powerful method for exploring surfaces and interfaces. As a second order nonlinear optical process under the electric dipole approximation, SFG is only sensitive to a medium without inversion symmetry.[3] Thus, a gas solid interface is an ideal situation for SFG studies. In SFG, a tunable wavelength infrared laser beam is mixed with a fixed wavelength visible laser beam on the surface to generate a sum frequency signal. Through SFG vibrational spectra, one can deduce the presence and orientation of molecules adsorbed onto the surface with submonolayer sensitivity. Furthermore, the use of pulsed lasers in SFG allows for time resolved measurements.

In this work, experiments were conducted to elucidate the interaction of adsorbed molecules of carbon monoxide, ethylene and propylene on Pt(111) at high pressures and temperatures. This study is done through the conventional SFG methods carried out previously in this research group as well as by using two infrared and one visible laser beams to detect two different surface species simultaneously. To carry out this work, a second-generation ultra high vacuum-high pressure reaction system and a laser system designed for simultaneous observation of two surface species at two different spectral regions were constructed.

The first system under study is CO on Pt(111) at high pressures and temperatures. The CO on platinum system is probably the most studied model system due to its supposed simplicity. Furthermore, this system is vital to understanding CO oxidation, a component of the automobile catalytic converter process. With vast amounts of attention paid to this model system, little is still know about its behavior under high pressures and temperatures; a result of limited high-pressure, in situ techniques. The SFG study will focus on heating the Pt(111) single crystal under high pressures of CO to examine whether any novel CO surface species form or dissociate to form carbon. In addition, the room temperature high-pressure system will be revisited to correct for improper normalization schemes that occurred in the past.

Our second high-pressure study will be on the coadsorption systems of CO ethylene as well as CO propylene. The coadsorption system is interesting because surface processes under real world conditions often involve multiple adsorbed species, as in the case of poisons and promoters in heterogeneous catalysis. The study on how concentration differences of coadsorbed species relative to each other will affect their interaction will offer insights to the role gas impurities play in reactions. To this end, the role of CO as a poison in ethylene hydrogenation on Pt(111) will be examined. To carry out all the studies regarding coadsorption, both CO and its complementary partner of ethylene or propylene will be observed simultaneously through the use 2-IR and 1-visible laser beams.

In this dissertation, the first section will be on UHV experimental methods including sample preparation and the various UHV surface techniques of Auger electron spectroscopy, low energy electron diffraction, and temperature programmed desorption. Following, SFG theory will also be discussed. Afterwards, the instrumentation section will include the laser setup and its automation, the construction of the UHV-high pressure reaction cell, and the programs used for interfacing the computer to the Auger and mass spectrometer. Subsequently, the systems studied will be presented in the order described previously.

References

1. G.A. Somorjai, Chemistry in Two Dimensions: Surfaces. 1981, Ithaca, NY: Cornell University Press.
2. P.C. Cremer, X. Su, Y.R. Shen, G.A. Somorjai, J. Phys. Chem., **100,** 16302, (1996).
3. Y.R. Shen, Nature, 337, 519, 1989

Chapter 2

UHV experimental methods

A. Working in ultra high vacuum

The detailed study of adsorbates on surfaces requires the availability of an UHV environment to clean, and characterize the surface. To maintain a clean surface, the following calculation gives an estimate to the necessary conditions.

$$\text{Flux (molecules/cm}^2\text{ sec)} = \frac{3.51\text{x}10^{22}\,P(torr)}{(M(g/mole)T)^{1/2}} \qquad (1)$$

where P is the pressure of the gas in torr and M is the molar mass of the molecule.[1] CO on a platinum surface at room temperature will be used as the example where a molecule sticks to the surface each time it strikes. In these conditions, the flux of molecules arriving on the surface at 1 torr is $3.88\text{x}10^{20}$ molecules $\text{cm}^{-2}\ \text{s}^{-1}$ and since 1cm^2 of the surface has approximately 10^{15} atoms, the amount of time needed to cover the surface with 1 monolayer of CO is about 3×10^{-6} s. This means that the pressure has to be below 10^{-9} torr to maintain a relatively clean surface for about 1 hour. From this basis, the Langmuir (1L =

$1x10^{-6}$ torr sec) unit is derived to represent the exposure corresponding to one monolayer coverage. In order to attain these low pressures, a stainless steel UHV chamber is used. The most popular method to pump the chamber to UHV involves the combination of turbo molecular pumps, ion pumps and titanium sublimation pumps. This combination offers ease of use with relatively no maintenance when compared to oil diffusion pumps that require regular LN_2 "feedings". Another critical component that is necessary to attain the desired pressure inside the chamber is to "bake" the whole chamber. Normal outgassing due to desorption of adsorbed gasses from the inner chamber walls and instrument surfaces limits the pressure we can achieve. During the baking process, which involves heating the chamber to between 120-200^{o} C for 48 hours, the desorption rate of gasses from theses surfaces is increased.

B. Sample preparation

Starting with a metal single crystal boule from a commercial source (Goodfellows), the boule is checked with Laue to ensure that the orientation is to within 2^{o} of the preferred crystal plane. In addition, the crystal is checked for twinning within the crystal. By mounting the boule in a goniometer and attaching the goniometer to the optical rail on the diffraction unit, the boule can be aligned to be within 0.5^{o} of the crystallographic axis. After finding this orientation, the boule and goniometer are mounted on an Electro-Discharge Machine to be sliced to 1mm thickness as individual samples. After obtaining the individual samples,

they are mounted onto a phasing goniometer for reorientation on the Laue prior to final polishing. After obtaining the desired orientation on the phasing goniometer, the crystal is set parallel to the front face of the goniometer. In this setting, the front surface of the crystal is ground flat staring with 0 emery grade paper and working to 0000 emery grade paper. After grinding with the 0000 emery grade paper, the scratches on the surface are on the order on 30 microns. After final grinding on the emery grade paper, the crystal is dismounted from the goniometer and the crystal is set in Koldmount epoxy for further polishing. Additional polishing of the crystal is done on a polishing wheel with a napless cloth and diamond paste. Starting with 30 micron diamond paste, the grit size is decreased to 6 microns, then 1 micron, and finally 0.25 microns with fresh polishing cloth with each change of grit. After polishing with the 0.25 micron paste, the crystal is ready to be introduced into the chamber. The crystal can be separated from the epoxy either by dissolving in acetone and sonication or if the sample is Pt, it can be heated in a hydrogen flame. Heating the crystal in the hydrogen flame will remove bulk contaminates. In the UHV chamber, multiple cycles of Ar^+ sputtering combined with annealing in O_2 will remove the majority of the surface contaminates, which can be checked by Auger spectroscopy.

Since a Pt(111) single crystal was used for the entirety of this work its specific cleaning conditions after the prolonged sputtering and oxygen treatments will be described. The Pt(111) crystal is cleaned by three cycles of 12 minute argon sputtering ($3x10^{-5}$ torr Ar pressure, 1000 volts, and 20 mA emission

current) and heating in oxygen (5x10-7 torr O_2, 1123K). As the last step of the cleaning cycle following the oxygen treatment, the sample was annealed for 2 minutes at $2x10^{-9}$ torr and 1133K to form a clean and well-ordered surface.

C. Auger electron spectroscopy

Auger Electron Spectroscopy (AES) is an electron in electron out method to provide surface chemical composition. Its surface sensitivity comes as a result of the limited depth penetration of electrons. As electrons with incident energy of 2000-3000 eV impact the surface, a core electron is ejected. As an outer shell electron decays to fill the inner core hole, an X-ray photon can be emitted via X-ray fluorescence or an Auger electron can be ejected as a result of the energy being transferred to an even shallower electron. This process is illustrated in figure 2.1. It should be noted that the Auger process is not an internal photoelectron process where an X-ray photon created from the initial core hole ejection ejects an Auger electron. In the Auger process, the selection rules for changing the orbital angular momentum quantum number by ±1 does not apply as it does in optical transitions. The Auger process is nonradiative and depends on electrostatic forces between a hole and the surrounding electron cloud.

The kinetic energy of the ejective electron in the nonradiative Auger process is given by:

$$KE = E_K - E_{L1} - E_{L3} \quad (2)$$

While the energy of the X-ray photon in X-ray fluorescence is given by:

$$h\nu = E_K - E_{L3} \quad (3)$$

For the Auger process, equation 2 only approximates experimental values because factors such as work function of the sample, work function of the spectrometer, and chemical shifts. When comparing the efficiencies between the two competing processes, the nuclear charge greatly affects their yields.

$$\text{Auger Yield} = \frac{1}{1+\beta Z^4} \quad (4)$$

$$\text{X-ray Yield} = \frac{\beta Z^4}{1+\beta Z^4} \quad (5)$$

Where Z is the nuclear charge and β is an experimentally determined parameter. The dependence of the yield to nuclear charge indicates that the Auger process dominates in lighter atoms and is equal to that of X-ray fluorescence at Ge (Z=32). In chemical identification, the short mean-free-path of the ejected Auger electrons (from 10-1000 eV) offer surface sensitivity whereas the emitted X-rays in X-ray fluorescence has a long mean-free-path so it is more appropriately used

for bulk chemical characterization. Further detailed descriptions of theses processes can be found in several references.

To collect Auger spectra, an electron gun and electron energy analyzer are needed. For this work, a PHI 10-155 cylinder mirror analyzer (CMA), which integrates the electron gun with the analyzer, was used. In a CMA, an on axis electron gun is located in the center of the instrument. The electron gun produces a 2000 eV electron beam that is used to generate the core hole in the Auger process. The generated Auger electrons will be collected by the CMA and focused onto the detector by static electric fields. This focusing process requires the use of two concentric cylinders. The cylinders are separated with ceramic electrobreaks since the inner cylinder is held to ground while the outer cylinder is biased at a variable negative voltage. As Auger electrons enter the entrance aperture between the two cylinders, it is attracted to the inner cylinder and its initial trajectory is altered. By varying the outer cylinder potential, electrons with the desired kinetic energies can be set to pass an exit aperture. As the electron passes the exit aperture it strikes a channeltron for amplification. To separate the large quantities of inelastically back scattered and secondary electrons from the small Auger signals, a lock-in amplifier is used. The CMA pass energy is modulated at 3 kHz with 2 V amplitude. The high pass frequency filter allows the signal current to be decoupled and detected with the lock-in amplifier.

D. Low energy electron diffraction

Low energy electron diffraction (LEED) is used commonly to detect long range order of single crystal substrates and their adsorbates. In LEED, a monochromatic beam of electrons between 20-500 eV is directed onto a single crystal metal surface. Some electrons backscatter and strikes a fluorescent screen used to detect the electrons. The scattering process in LEED is illustrated in figure 2.2. Due to the wave nature of the electrons as described by de Broglie,

$$\lambda = \frac{h}{\sqrt{2m_e E}} \tag{6}$$

where λ is the electron wavelength, h is Planck's constant, m_e is the mass of an electron, and E is the energy of the electron, some of the back scattered electrons will be diffracted. The diffraction spots observed give a reciprocal space representation of the two dimensional surface periodicity. The wave nature of electrons in conjunction with translational symmetry restrictions of the crystal allow momentum transfer to values of integer multiples of a reciprocal lattice vector. The two dimension diffraction process can be described by a one dimensional infinite line of scatters as illustrated in figure 2.3. In this picture, plane waves are scattered off a one dimensional lattice with a periodicity of a. For the beams to interfere constructively, the difference in the path length

between scatters at two adjacent lattice points must be equal to the integer multiples of the electron wavelength.

$$a (\sin \theta_s - \sin \theta_i) = n\lambda \quad (7)$$

While equation 7 describes scattering from a line in the one dimension case, scattering in two dimensions occur in a plane. The diffraction in two dimension is described in the 2 dimension reciprocal lattice. The reciprocal lattice vectors $\vec{b}_1$, $\vec{b}_2$ is related to the real space vectors $\vec{a}_1$, $\vec{a}_2$ by,

$$\vec{a}_i \bullet \vec{b}_j = 2\pi\delta_{i,j} \text{ (i,j,=1,2)} \quad (8)$$

where $\delta_{i,j}$ is the Kronecker delta function ($\delta_{i,j} = 0$ if $i \neq j$ and $\delta_{i,j} = 1$ if $i=j$). The Laue conditions for LEED are:

$$\vec{a}_1 \bullet (\vec{k}_s - \vec{k}_i) = 2\pi n_1 \quad (9)$$

$$\vec{a}_2 \bullet (\vec{k}_s - \vec{k}_i) = 2\pi n_2 \quad (10)$$

where $\vec{k}_s$ is the scattered wave vector and $\vec{k}_i$ is the incident wave vector and n_1 and n_2 are integers. In figure 2.4, several examples of how the real space structure translates to the diffraction patterns are shown. Depicted are fcc (111) surfaces

with hexagonal structure showing both the clean surfaces fcc(111)-(1x1) as well as when a 2x2 overlayer of adsorbates are covering the surface.

E. Temperature programmed desorption and residual gas analysis

A mass spectrometer is used to monitor gasses in the chamber. Through the mass spectrometer, we can perform temperature programmed desorption (TPD) experiments as well as conduct residual gas analysis (RGA). TPD experiments can determine adsorbate composition by heating the substrate until adsorbate species desorb off the surface. RGA is used to check for leaks, as well as detecting the composition of gasses that will adsorb onto the substrate as contaminants.

An UTI-100C quadrupole mass spectrometer was used to collect all the mass data. In order to detect the mass of atoms and molecules, the first step is to for those species to undergo ionization. Ionization of theses species are done by 70 eV electrons emitted from a heated helical tungsten filament. After ionization, the positively charged species are directed toward a radio-frequency (RF) quadrupole mass selector. The quadrupole mass selector consists of four molybdenum cylindrical rods. The quadrupole mass selector acts as a band pass filter by combining a high pass filter formed by two of the rods with a low pass filter formed by the other two rods. The high pass filter is formed with 2 of the rods biased with a positive DC potential and an oscillating RF field whose peak-

to-peak amplitude exceeds the DC voltage. In this matter, the heavy species with high m/z ratios will be unaffected by the fluctuating RF field while the lighter species will be attracted to the rods and filtered. For the low pass half, the opposite occurs where the RF field is coupled to a negatively biased set of rods. In this matter, the heavy species are attracted to the poles and the lighter ones are able to a find a stable oscillatory path through the filter. Passing through the mass selector, the positively charged species strike a negatively charged channeltron. The channeltron amplifies the secondary electrons generated upon impact and the current signal is converted to voltage, which is read by the computer.

To perform TPD experiments, the sample is heated linearly and the mass spectrum signal is collected as a function of the temperature. With proper programming, the mass spectrometer can be set for multiple mass detection. In addition to identifying the adsorbed species from the surface TPD can also gives data on the binding energy of the adsorbed species. Rapid pumping of the chamber and the mass spectrometer is necessary because the pump rate has to exceed the desorption rate of the surface species during the heating ramp. Under this condition, the signal from the mass spectrometer is directly proportional to the rate of desorption with respect to time.

In addition to TPD experiments, the mass spectrometer can be used for RGA of the vacuum system's environment. RGA is extremely important for determining leak into the chamber. By looking for the presence of oxygen (mass 32 and 16) and nitrogen (mass 14 and 7) as a major component of the background

gasses, it can be determined as to whether a leak is present. If a leak is present, RGA can be set to detect for minute traces of helium, which is used from the outside as a method to pinpoint the position of the leak. In addition, RGA checks for the general cleanliness of the chamber to determine whether oil back streams from mechanical backing pumps. Another area for RGA is during gas dosing. Gasses are dosed into the vacuum chamber during sputtering, heating, and for adsorption studies. Its purity can be check by RGA. Finally, in the RGA mode, a small amount of reaction gasses can be leaked from the high pressure cell into the UHV chamber during an experiment for composition analysis as a function of time. In this fashion, the data can be used to determine the rate of the reaction.

References

1. D.P. Woodruff and T.A. Delchar, *Modern techniques of surface science*. (Cambridge University Press, 1986)
2. G.A. Somorjai, *Introduction to Surface Chemistry and Catalysis*. (JohnWiley & Sons Inc., 1993)
3. G. Ertl and J. Kuppers, *Low energy electron and surface chemistry*. (Weinheim: Verlag Chemie, 1974)
4. M.A. Van Hove, W.H. Weinberg and C.H. Chan, *Low energy electron diffraction: experiment, theory, and surface structure determination.* (Springer: Verlag Berlin, Heidelbery, 1986).

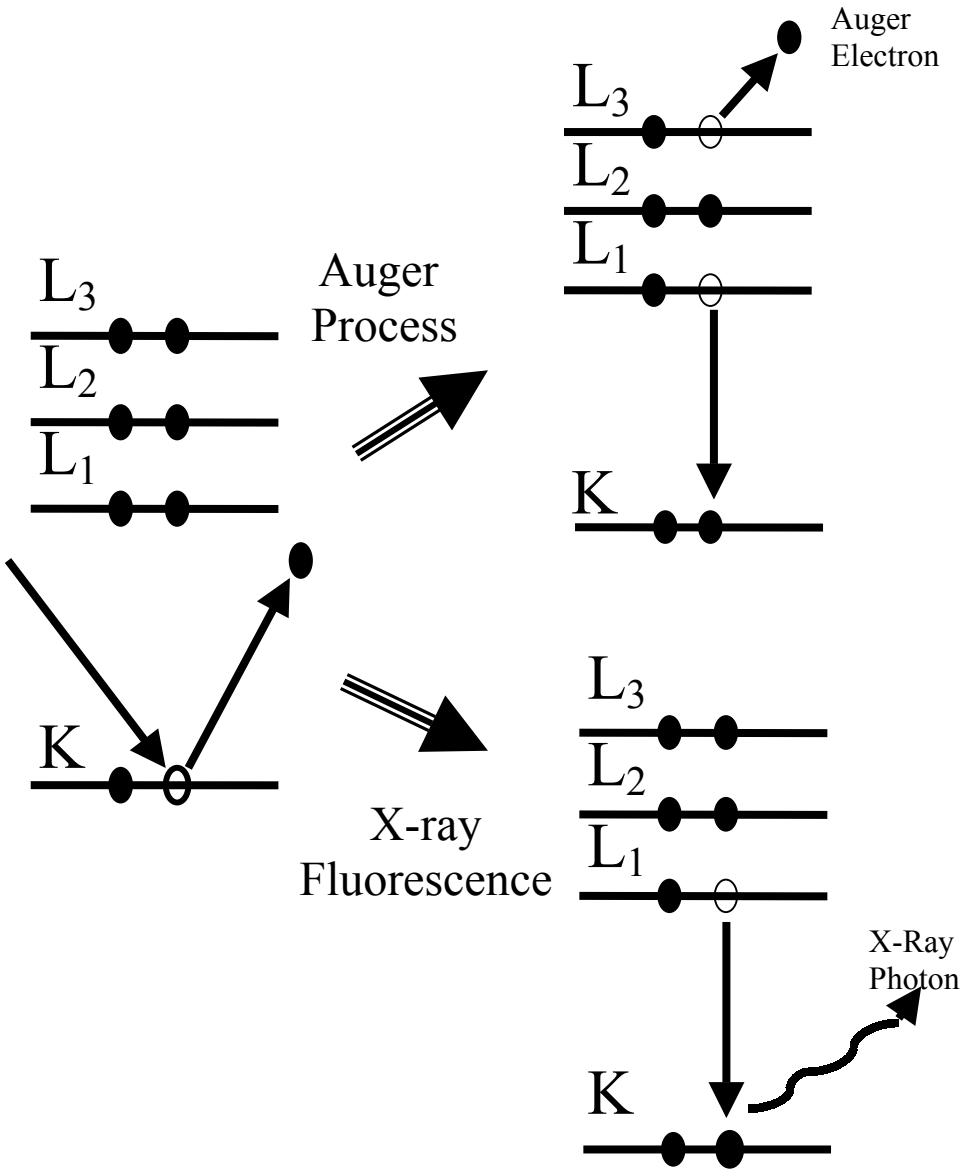

Figure 2.1 Illustration of the Auger electron process. After core hole creation by a high energy electron beam, decay from an outer shell electron can cause either the Auger process or X-ray fluorescence.

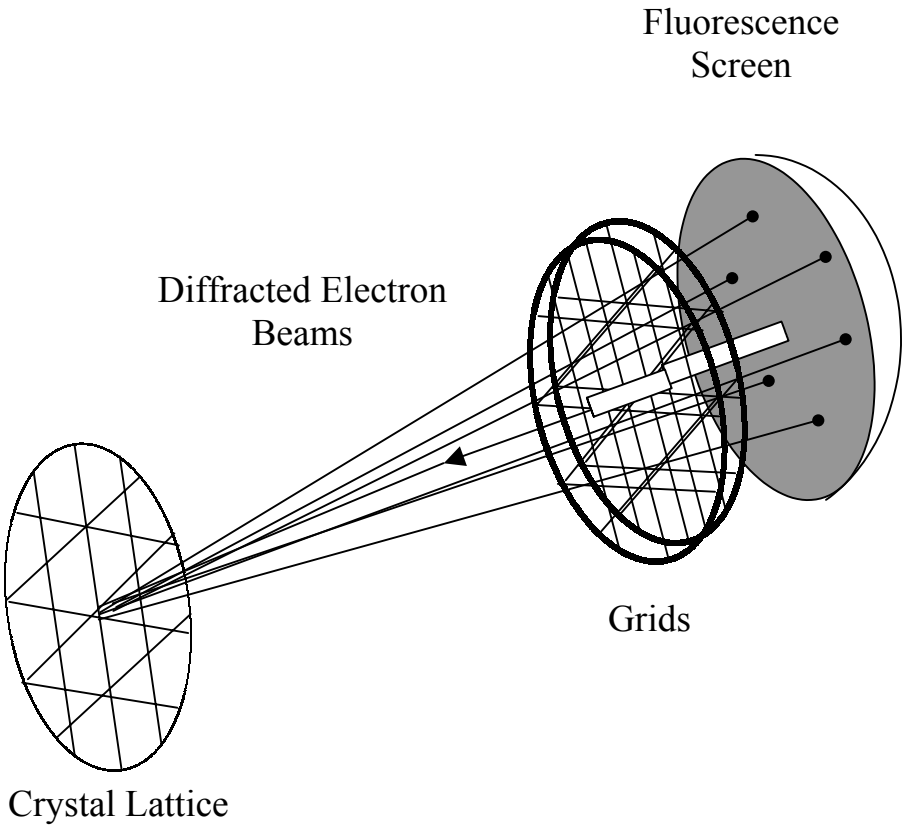

Figure 2.2 A representation of the scattering process in the LEED experiment. Monoenergetic electrons generated in the electron gun are scattered off the lattice of the crystal. Only the scattered electrons will pass through the grids to strike the fluorescence screen on which the impact position can be screen. The arrows represent the possible paths of electrons.

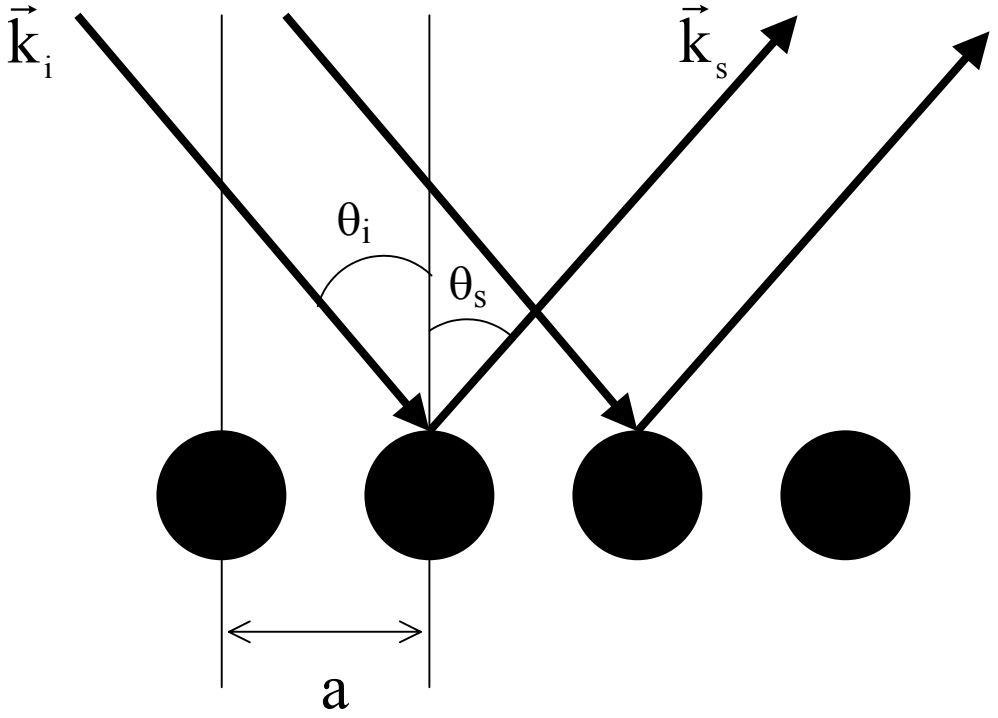

Figure 2.3 Scattering of an electron plane wave off a one dimensional lattice.θ_i and θ_s are the incident and scattered angles respectively. k_i and k_s are the incident and scattered wave vectors. a is the lattice spacing.

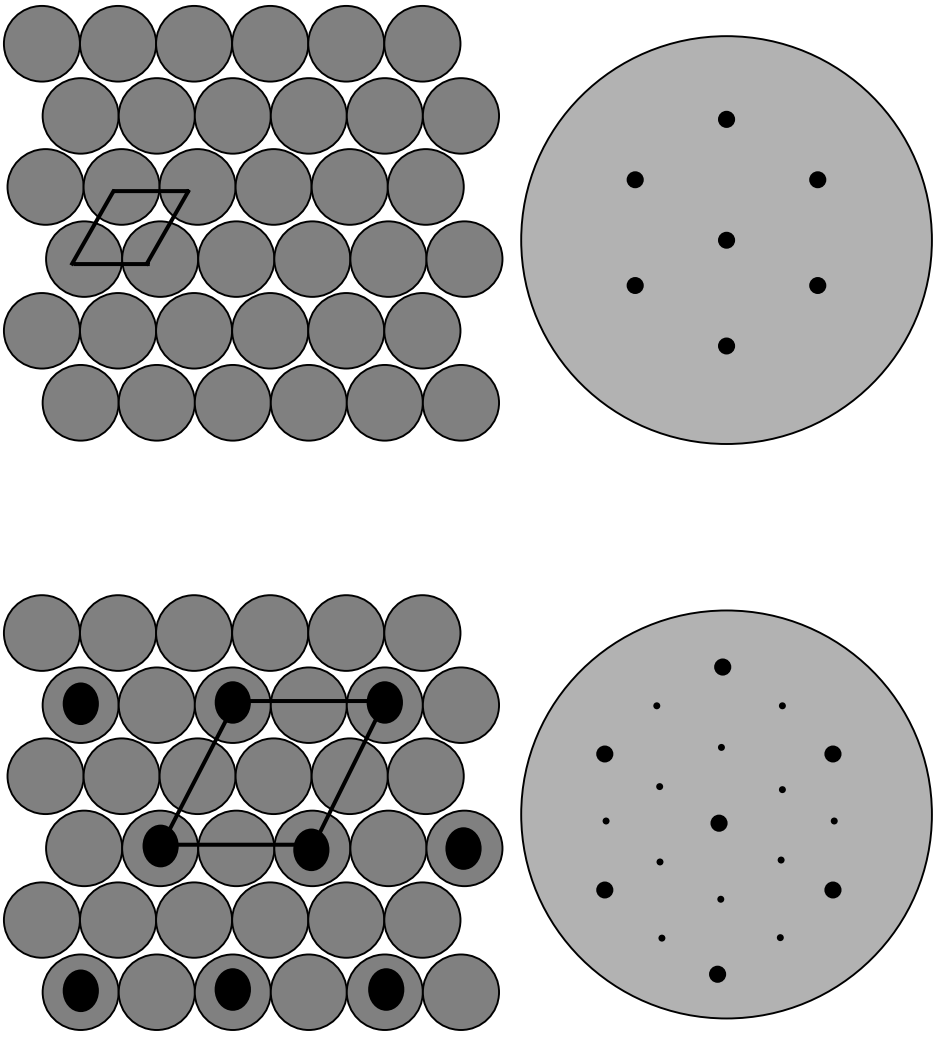

Figure 2.4 An illustration of the real space lattice and its diffraction pattern of an fcc(111)-(1x1) surface indicative of a clean surface and from a 2x2 overlayer.

Chapter 3

Sum Frequency Generation Theory

With the advent of high power pulsed lasers, nonlinear optical techniques have become available to the study of surfaces and interfaces. The need to probe surface and interface in the presence of bulk medium is necessary to conduct experiments in real world conditions. Second order nonlinear optical spectroscopy of infrared visible sum frequency generation (SFG) is ideal for this task because through symmetry and under the electric dipole approximation, this process is forbidden in a medium of inversion symmetry. A surface or interfaces necessarily breaks this symmetry requirement and becomes available for SFG studies. As an optical process, it is accessible to any surface that is available to light, thus allowing in situ studies ranging from gas solid interfaces to buried liquid and solid interfaces.

Infrared visible sum frequency generation shows excellent sub-monolayer sensitivity to adsorbates on the surface because it is a vibrational technique. SFG involves probing of the interface with a tunable infrared laser beam while the fixed wavelength visible laser beam up-converts the signal to the visible regime. Under this arrangement, the visible signal may be detected by photomultiplier tubes (PMT) which have excellent sensitivity in this regime. Since SFG is a second order process involving infrared and visible transitions, its sensitivity is

restricted to adsorbates that possess both infrared and Raman activity. In 1987, X.D. Zhu et al. demonstrated the first successful experiment in infrared visible sum frequency generation. It should be noted that a similar process, second harmonic generation (SHG), also posses the inherent surface sensitivity but the lack of commercially available mid-infrared PMT detectors restricts it use in vibrational studies. This chapter will examine the basic theory of SFG as it applies to the study of gas metal interfaces.

Sum frequency generation is a three wave mixing process whereby two input electric fields interact with a surface or a medium without inversion symmetry and generate an output frequency that is the sum of the input fields. This is depicted in figure 3.1. The interaction can be described by:

$$\omega_{SF} = \omega_{IR} + \omega_V \tag{1}$$

where ω_{IR} and ω_V are the input fields for the infrared and visible respectively and ω_{SF} is the resulting sum frequency signal. In a medium without inversion symmetry, two input fields under the electric dipole approximation will induce a second order polarization proportional to the sum of the two input fields. This is described by the equation:

$$\vec{P}^{(2)}_{\omega_{SF}} = \chi^{(2)} : \vec{E}_{\omega_{IR}} \vec{E}_{\omega_v} \tag{2}$$

where $\chi^{(2)}$ is the second order susceptibility tensor. From equation two one can see that the second order susceptibility tensor, which is a third rank tensor, depends on the symmetry properties of the medium. For bulk medium possessing complete inversion symmetry, $\chi^{(2)} = -\chi^{(2)} = 0$ thus all of the tensor elements are zero. This indicates that SFG is inherently insensitive to the bulk medium. On the surface however, the inversion symmetry is necessary broken so $\chi^{(2)} \neq 0$. This surfaced susceptibility allows for the high degree of surface specificity in the SFG experiments.

In the SFG experiments, the sum frequency signal can be expressed as a function of the $\chi^{(2)}$ in terms of photons per pulse:

$$S(\omega_s) = \frac{8\pi^3 \omega_s^2 \sec^2 \theta_s}{\hbar c^3 n(\omega_s) n(\omega_v) n(\omega_{IR})} | e(\omega_s) \cdot \chi^{(2)} : e(\omega_v) e(\omega_{IR}) |^2 \; I_v I_{IR} AT \qquad (3)$$

where I_{IR} intensity of the infrared input beam, I_V is the intensity of visible input beam, A relates to the beam overlapping cross section at the interface, T is the pulse width, θ_S is the reflection angle of the SFG beam from the surface normal, $n(\omega)$ is the frequency dependent refractive index of the medium, $\chi^{(2)}$ is the effective surface nonlinear susceptibility and $e(\omega)$ is the dot product of the unit vector describing the polarization of the optical field at frequency ω and the corresponding Fresnel coefficients. While $\chi^{(2)}$ represents the macroscopic

susceptibility, it is related to the microscopic molecular polarizability $\alpha^{(2)}$ through:

$$\chi_{ijk}^{(2)} = N \cdot \sum_{l,m,n} < (i \cdot l)(j \cdot m)(k \cdot n) > \alpha_{lmn}^{(2)} \quad (4)$$

where N is the number density of species on the surface, <(i·l)(j·m)(k·n)> represents the coordination transformation from the molecular reference frame to the macroscopic lab frame averaged over the molecular orientation distribution. The indices ijk or lmn refers to the sum frequency, visible, and infrared components respectively.

From second order perturbations theory, the molecular susceptibility $\alpha_{lmn}^{(2)}$ can be separated into a resonant $\alpha_{lmn}^{(2),R}$ and a non-resonant term $\alpha_{lmn}^{(2),NR}$ by:

$$\alpha_{lmn}^{(2)} = \alpha_{lmn}^{(2),R} + \alpha_{lmn}^{(2),NR} \quad (5)$$

The resonant portion can be expressed as:

$$\alpha_{lmn}^{(2),R} = \frac{1}{\hbar}\sum_{v}\sum_{v'}\left[\frac{\hat{\rho}gv', gv\left\langle \Psi_{gv'} \mid \mu_n \mid \Psi_{gv}\right\rangle}{(\omega_{gv',gv} - \omega_{IR}) - i\Gamma_{gv',gv}}\right]\left\langle \Psi_{gv} \mid \alpha_{lm}^{(1)} \mid \Psi_{gv'}\right\rangle$$

$$= \frac{1}{\hbar}\sum_{v}\sum_{v'}\left[\frac{\hat{\rho}gv', gv\left\langle \Psi_{gv'} \mid \mu_n \mid \Psi_{gv}\right\rangle}{(\omega_{gv',gv} - \omega_{IR}) - i\Gamma_{gv',gv}}\right]M_{lm}$$

where (6)

$$M_{lm} = \sum_{p}\left[\frac{\left\langle \Psi_{gv} \mid \mu_1 \mid \Psi_p\right\rangle\left\langle \Psi_p \mid \mu_m \mid \Psi_{gv'}\right\rangle}{(\omega_{p,gv'} - \omega_{SF})} - \frac{\left\langle \Psi_{gv'} \mid \mu_1 \mid \Psi_p\right\rangle\left\langle \Psi_p \mid \mu_m \mid \Psi_{gv}\right\rangle}{(\omega_{p,gv'} + \omega_{SF})}\right]$$

where g represents the ground electronic state, v is the initial vibrational state, v' is the final vibrational state, $\hat{\rho}$ is the density matrix, $\left\langle \Psi_{gv'} \mid \mu_n \mid \Psi_{gv}\right\rangle$ is the electric infrared dipole transition matrix element from the ψ_{gv} to $\psi_{gv'}$ state, $\omega_{gv',gv} = (E_{gv'}-E_{gv})/\hbar$ is the vibrational frequency for the state energy difference between the gv state (E_{gv}) and the gv' state ($E_{gv'}$), $\Gamma_{gv',gv}$ is the phenomenological damping constant of the gv to gv' transition, $\alpha_{lm}^{(1)}$ is the polarizability tensor, M_{lm} is the Raman matrix element describing the transitions between Ψ_{gv} and $\Psi_{gv'}$ through the intermediate states Ψ_p, and $\omega_{p,gv}$ is the frequency associated with the transition from the Ψ_{gv} state to the Ψ_p state. This process can also be thought of as coupling the incident infrared field to the infrared dipole transition, which then is up-converted by the Raman process described by the Raman matrix M_{lm}. This can be represented by:

$$\alpha_{lmn}^{(2),R} = \sum_{Q} \frac{A_Q \Delta\rho_{Qg}}{(\omega_Q - \omega_{IR} - i\Gamma_Q)}$$

where (7)

$$A_Q = \frac{1}{2\omega_Q} \frac{\partial \mu_n}{\partial q} \frac{\partial \alpha_{lm}^{(1)}}{\partial q}$$

and $\Delta\rho_{Qg}$ is the difference between the ground and first excited vibrational state Q. $\frac{\partial \mu_n}{\partial q}$ is the infrared dipole moment derivative, and $\frac{\partial \alpha_{lm}^{(1)}}{\partial q}$ is the Raman polarizability for the particular vibrational mode Q with respect to the normal coordinate q. The above equations represent the gross selection rules for the infrared visible SFG process that requires modes to be both infrared and Raman active. In medium with total inversion symmetry, symmetry restrictions prohibit the existence of modes that are both infrared and Raman active. At the surface, this gross selection is satisfied thus making SFG a surface sensitive technique.

In SFG studies, the infrared beam is tuned across the vibrational transition of the interested surface species. In addition to the resonant feature arising from the surface species, a non-resonant response from the surface can also occur. The combination of these two responses may distort the normal Lorentzian lineshape characteristic of linear infrared spectrum. Depending on whether the non-resonant background interferes in a constructively or destructively with the resonant peak, a bump or dip may occur in the spectrum. In figure 3.2, interference of the resonant and nonresonant background where the ratio of the

two oscillator strengths are equal are displayed. The phase at 0, 90, 180, and 270 degrees are shown. In figure 3.3, interference of the resonant and nonresonant background where the ratio of the nonresonant term is 5% of the resonant term. The phase at 0, 90, 180, and 270 degrees are shown. In cases where the lineshapes are distorted as result of interference or broadening, fitting of the sum frequency peaks must be done to obtain the correct peak frequency and linewidth. Since the sum frequency intensity and lineshape is proportional to the square of $\chi^{(2)}$, the peak is fitted to $\chi^{(2)}$ after taking into account the resonant and non-resonant portions.

$$\begin{aligned} \chi^{(2)} &= \chi_R^{(2)} + \chi_{NR}^{(2)} \\ \chi_R^{(2)} &= \sum \frac{A_Q}{\omega_{IR-\omega_Q+i\Gamma_Q}} \\ \chi_{NR}^{(2)} &= ke^{i\phi} \end{aligned} \tag{8}$$

where the non-resonant term possesses a phase dependence term.

As a third rank tensor, the second order nonlinear susceptibility $\chi^{(2)}$ consists of 27 elements that are properties of the medium. On a surface, many of these elements vanish due to symmetry relations. In the case of an isotropic surface, there are four nonvanishing terms which remain after rotational and reflection symmetries are considered. These four terms are: $\chi_{xxz}^{(2)} = \chi_{yyz}^{(2)}$, $\chi_{zxx}^{(2)} = \chi_{zyy}^{(2)}$, $\chi_{xzx}^{(2)} = \chi_{yzy}^{(2)}$ and $\chi_{zzz}^{(2)}$. In an SFG experiment, the use of different

polarization combinations allows the different tensor elements to be probed and molecular orientation of the surface species may be deduced. The input laser beams are polarized either s or p whereby s refers to polarization in the plane of the surface and p refers to polarization out of the plane of the surface. Moving from the laboratory to the molecular frame, the s-polarized beams has only an s component whereas the p polarized beam can be decomposed in an s and p component. The choice of the two input beam polarization combinations forms 4 possible combination. Of theses 4 combination, only ppp which refers to the polarization of the sum frequency beam, visible beam and infrared beam in order of energy, was used to probe the metal surface. Due to the metal surface selection rules, dipoles along the metal surface can not be excites as a result of the metal image dipole. The electric field of the s polarized infrared beam is cancelled by the image field of electrons from the surface. As a result, only p polarized infrared beam is used in these experiments. Since the visible beam is related to the polarizability, it can be in s or p polarization. However, the local field intensity of the p-polarized beam is greater than the s-polarized beam. In all of the SFG experiments presented in this thesis, ppp geometry was used unless otherwise noted.

References

1. Y.R. Shen, *The principles of nonlinear optics,* Wiley, New York, 1984.
2. A. Yariv, *Introduction to optical electronics*, Holt, Rinehart and Winston, Inc, 1971.
3. Y.R Shen, Nature **337**, 519, (1989).
4. Zhang, J. Y.; Huang, J. Y.; Shen, Y. R. *Optical Parametric Generation and Amplification*, 1st ed.; Harwood Academic Publishers: Luxembourg, 1995; Vol. 19.
5. Y.R. Shen, Annu. Rev. Phys. Chem., 40, 327, 1989.
6. G. Herzberg, *Infrared and raman spectra of polyatomic molecules*, Van Nostrand, Princeton, NJ, 1945.

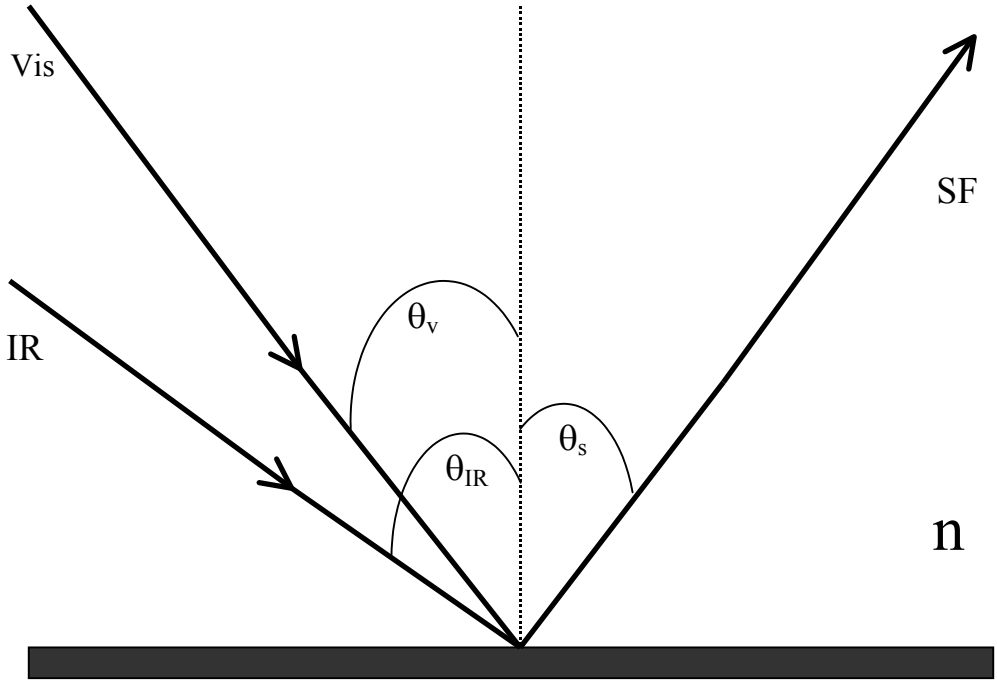

Figure 3.1 Geometry for sum-frequency generation from an interface in the reflected direction

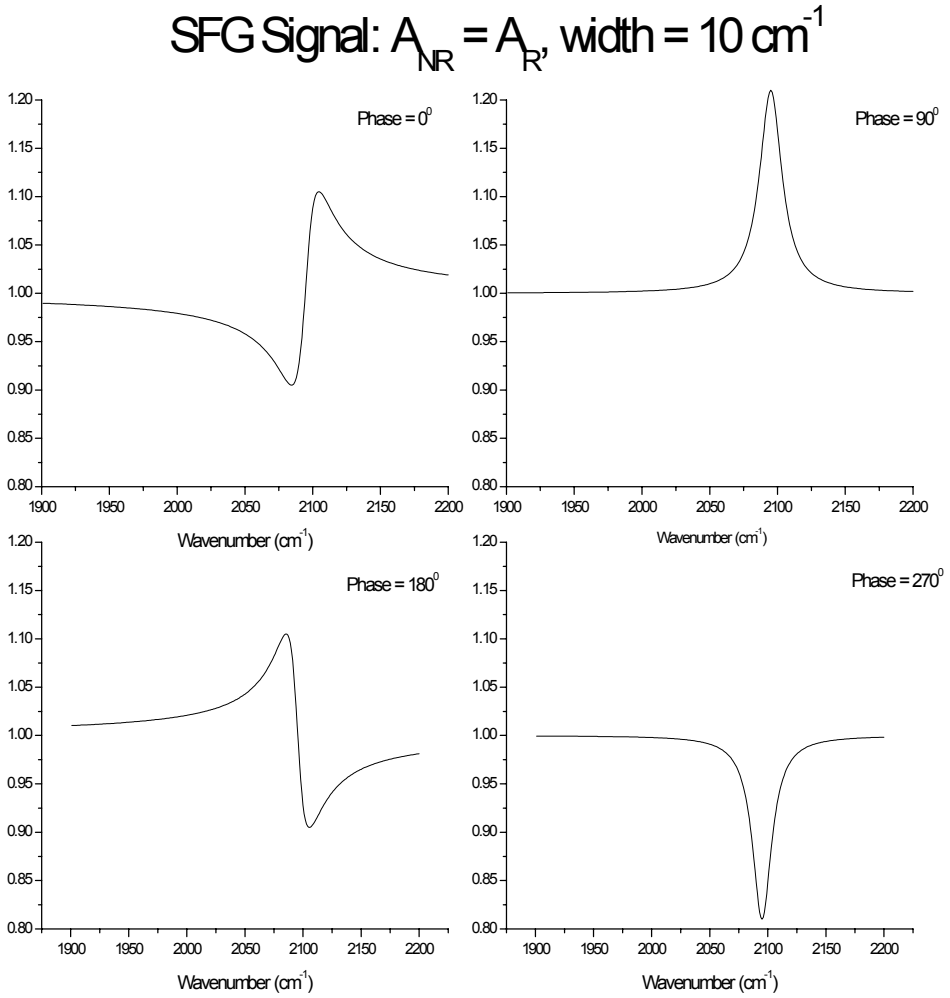

Figure 3.2 Interference of the resonant and nonresonant background where the ratio of the two oscillator strengths being equal. The phase at 0, 90, 180, and 270 degrees are shown.

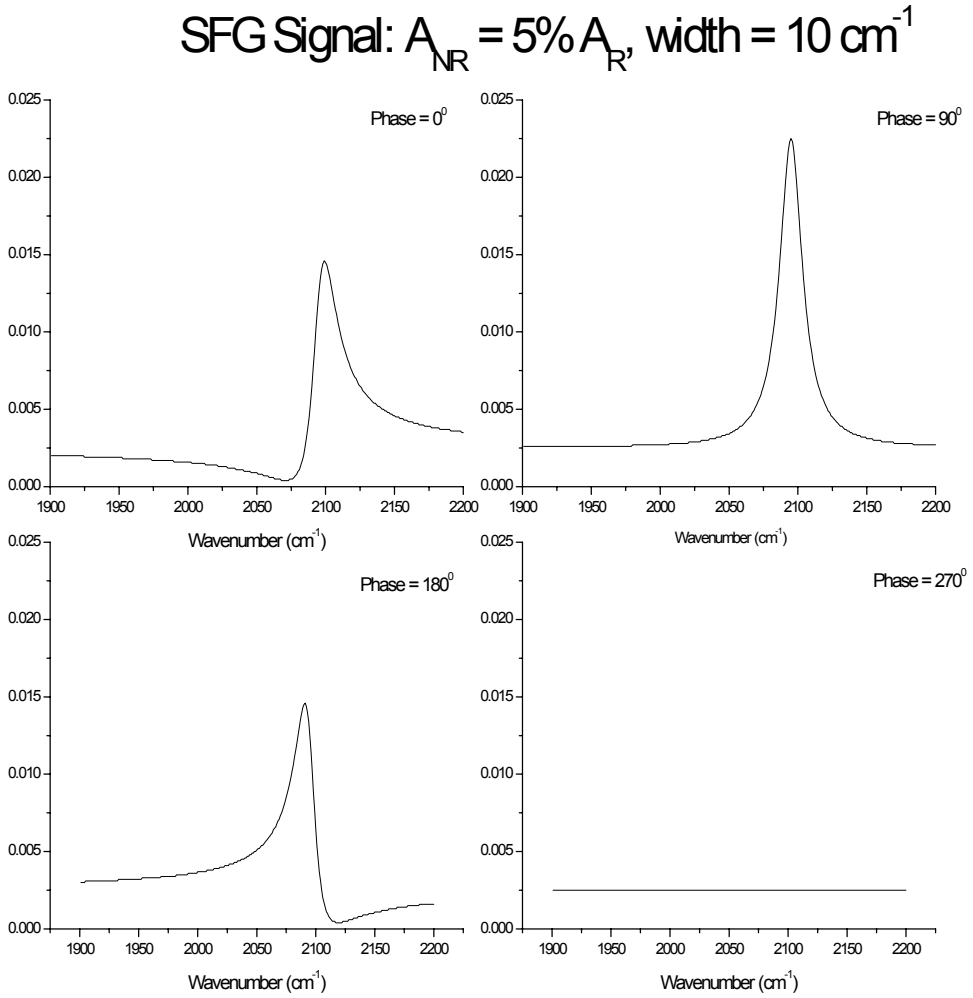

Figure 3.3 Interference of the resonant and nonresonant background where the ratio of the nonresonant term is 5% of the resonant term. The phase at 0, 90, 180, and 270 degrees are shown.

Chapter 4

Instrumentation

A. Laser setup and automation

All SFG experiments were carried out using a Nd:YAG based laser system. The heart of the laser system was a pulsed Continuum Nd:YAG Laser (PY61-C). This 20Hz, 20ps laser has its fundamental wavelength at1064 nm with output energy of 33mJ. The 1064 nm beam is used to pump 2 separate infrared optical parametric systems as well as produce the doubled 532 nm laser beam for the visible portion of SFG experiments. This laser system can be operated either in dual experiment mode, which allows two SFG experiments to be conducted separately and simultaneously or it can be operated in the 2-IR 1-visible mode to detect 2 species simultaneously in 1 experiment. All wavelength tuning are accomplished through rotation stages, which are controlled by a Labview data acquisition program.

In order to conduct two SFG experiments simultaneously with the same laser system, two optical parametric systems are needed to generate the separate tunable IR laser beams. For 2500-4000cm^{-1} range, a $LiNbO_3$ optical parametric generation and amplification stage (OPG/OPA) is used. For lower frequency requirements in the 1250-2500cm^{-1} range, a Beta Barium Borate (BBO)

OPG/OPA is used in conjunction with a $AgGaS_2$ (AGS) difference frequency generation (DFG) stage. If the laser system was used in the dual experiment mode and required two IR laser beams in the high frequency regime, the AGS crystal can be substituted with a $LiNbO_3$ crystal in the DFG stage. While generating two high frequency IR laser beams is possible, the system is limited to 1 AGS DFG setup for the low frequency region. The experimental setup for the whole laser system will be addressed in detail and is depicted in figure 4.1. The corresponding parts list as well as layout details are available in the appendix.

I. OPG/OPA with $LiNbO_3$

In nonlinear crystals, optical parametric oscillations, which involve the transfer of power from electromagnetic waves at different frequencies, can occur. In a nonlinear crystal, an intense laser beam at frequency ω_3 (pump) will generate 2 new laser beams at ω_1 (signal) and ω_2 (idler) such that $\omega_3 = \omega_1 + \omega_2$. The terms signal and idler refer to the output laser beams that has higher and lower energy respectively. In order to change the frequency of the output signal and idler laser beams, the nonlinear crystal is tuned to maintain phase matching conditions. As the angle of the nonlinear crystal is changed with respect to the input pump beam, a change in the refractive index is observed and phase-matching conditions ($\omega_3 n_3 = \omega_1 n_1 + \omega_2 n_2$) can be met.

In the $LiNbO_3$ stage, two $LiNbO_3$ crystals are used to carry out this nonlinear process. In the first $LiNbO_3$ crystal, OPG takes place and the infrared signal and idler is generated from the 1064nm pump beam. The second $LiNbO_3$ crystal serves two purposes, it takes the signal and idler as seed beams and carries out OPA to increase the infrared power level. In addition, the second crystal is counter rotated with respect to the first crystal to prevent beam walk off that occurs as the index of refraction changes during tuning. Approximately 10mJ of the 1064nm fundamental beam enters the OPG/OPA stage with 2mJ going to the OPG stage to generate the signal and idler beams at a combined energy of approximately 30μJ. The rest of the signal beam and the other 8mJ of 1064nm beam will combine with the signal and idler at the second $LiNbO_3$ crystal for OPA. The output tunable infrared laser beam (2.5-4μm) has approximately 300μJ of energy. The output infrared beam is vertically polarized and its polarization is rotated to horizontal with a MgF_2 waveplate. At the C-H stretch region of the infrared spectrum (approximately $2800cm^{-1}$), the infrared has about $15cm^{-1}$ bandwidth and about $30cm^{-1}$ bandwidth near the O-H stretch region (approximately $3600cm^{-1}$). To calibrate the frequency of the infrared laser beam, polystyrene and mica standards are used. Figure 4.2 show a sample infrared transmission spectrum of polystyrene taken with the $LiNbO_3$ syatem. To automate frequency tuning, the $LiNbO_3$ crystals are mounted on 5-axis gimbal mount and placed on top of computer controlled rotation stages. The rotation stages are controlled to run synchronously with the data acquisition program.

II. OPG/OPA/DFG with BBO and AGS

To produce IR in the longer wavelength region of 4-8μm, 4 nonlinear crystal are needed. The 1st step in the process is to generate 532nm laser beam from the YAG 1064 fundamental. This is accomplished by frequency doubling in an angle tuned LBO crystal. The second harmonic produced serves two purposes, to provide the visible portion of the SFG experiment as well as to pump the BBO OPG/OPA stage. At about 80% efficiency, approximately 16mJ of the YAG fundamental is converted to 13mJ of the second harmonic. From this 13mJ of 532nm beam, 2.6mJ is separated for the visible portion of the SFG experiment. The remaining 80% is sent to the BBO OPG/OPA stage. The setup for the BBO OPG/OPA stage is analogous to the $LiNBO_3$ setup except for a few noted differences. The laser beam makes a double pass through both BBO crystals rather than just one. In the 1st pass, OPG occurs at the 1st BBO crystal and is amplified at the second. Further amplification occurs as the beams pass back through both BBO crystals. In this 2nd pass amplification process, the linewidth of the idler beam has been narrowed through the use of a grating. After amplification, the pump and signal beams are all rejected and the leftover idler beam (approximately 1300nm) is sent to the AGS crystal for DFG. At the AGS crystal, the idler and a delayed 1064nm beam is combined for DFG and IR in the 4-8μm range is produced. The output of the infrared is vertically polarized and is

rotated to horizontal polarization by a MgF_2 waveplate. The IR energy in the CO stretch (approximately 2000cm^{-1}) region has about 150μJ of energy and line width of approximately 8cm^{-1}. To tune the IR, 4 rotation stages carrying the 2 BBO crystals, the AGS crystal and the grating have to be moved for each wavelength. The rotation stages are controlled by computer and run synchronously with the data acquisition program. To calibrate IR produced, gas phase CO, and CO_2 are used. One thing that should be noted about the AGS crystal is that it is extremely easy to damage. At all times when possible, the AGS crystal should be covered from room lights and under no circumstances should the 532nm laser beam ever be put through. Extreme care is requires in order to prevent silver migration which will cause the crystal to turn black and become ineffective.

For situations when a second $LiNbO_3$ setup is needed or when narrow line widths are required in the higher frequency region, a $LiNbO_3$ crystal can be put in place of the AGS crystal. In this situation the BBO OPG/OPA system outputs a difference IR idler to meet the wavelength requirements. Since wavelength selection is calibrated to the grating position, the interchanging process is an easy process that requires no recalibration. Once the grating is set at the desired wavelength the $LiNbO_3$ crystal can be exchanged and the only step is to maximize the output IR energy. This step is aided greatly by looking for energy depletion of the 1064nm pump beam after passing through the crystal.

III. Detection System

To detect the sum frequency signal generated from the surface, a photomultiplier tube (PMT) is used (figure 4.3). The PMT is housed in a black box that contains a focusing lens, monochromator and an interference filter covering the entrance to reject room lights from entering the box. Outside of the detection box are a polarizer and a 532nm notch filter to reject any 532nm light that accompanies the sum frequency signal. The PMT is operated at 1200 volts and the output signal is read by a SR250 boxcar integrator that is connected to a SR245 computer interface. For the 2-IR 1-Visible experiments, two complete detection setups are necessary. In addition to detecting the sum frequency signal, the infrared power is monitored through a joule meter. The infrared is detected at two separate locations; one is off the reflection from the entrance window to the high-pressure cell and the other infrared detector looks at the signal reflected off the crystal surface. The latter detection is used to normalize for gas phase absorption in high-pressure experiments.

IV. Labview programs for IR tuning and data acquisition

All of the programs used to control the laser tuning as well as collecting data are written in Labview (National Instruments). IEEE standard General

Purpose Interface Bus (GPIB) cables are used to connection the computer to all the instruments. There are 4 separate main programs that are used in the SFG experiments. One program controls the $LiNbO_3$ system and collects data. In this program, the computer has to control 2 rotation stages and read from the SR245 computer interface. Another program controls the AGS system and collects data. The AGS program controls 4 rotation stages and read from the SR245 computer interface. A third program controls both the $LiNbO_3$ system as well as the AGS system and collects data. This program controls all 6 rotation stages and read from the SR245 computer interface. The last program is a real time program used to look for the sum frequency signal. This program reads data from the SR245 and display a real time signal. Of the 4 programs, the first two are used during normal SFG experiments where only 1 infrared beam is needed. If two experiments are going to run simultaneously, two computers are need. The 3rd mentioned program is used during the 2-IR 1-Visible experiments where both infrared system are used on the same experiment simultaneously. During this experiment, only one computer is needed to run the experiment but 2 complete signal collection setups are required. A program flowchart is shown in figure 4.4 and the all four programs are presented in the appendix.

B. Design of the UHV-HP transfer system

Using an existing UHV chamber, the reaction cell and sample transfer system was added. These additions include a sample mount, the UHV docking mount,

the reaction cell with docking mount, and the transfer arm. The reaction cell is sealed from the UHV chamber by either 1 or 2 2-3/4 inch gate valves, depending on whether the reaction cell will be removed as a stand alone unit. The main issues considered in the design of this system were, heating and cooling through resistive contacts, reading temperature from a thermocouple spot welded to the back of the sample, reducing reaction volume and possible reactivity from the walls, and large clear aperture for the laser beams. Large clear aperture is important for SFG experiments because the input laser beams are approaching at non-collinear geometry. Other less complicated issues were attaching a gas chromatograph, recirculation pump, gas handling system and separate reaction cell pumping systems. With separate pumping and gas handling systems, the reaction cell can be pumped out to less than 10^{-9} torr in 30 minutes after being in atmospheric pressure.

I. The UHV chamber

The UHV analysis chamber is a commercial Varian 60L stainless steel chamber pumped by a 250 l/s ion pump, a titanium sublimation pump, and a 360 l/s Lybold turbo molecular pump (figure 4.5). After baking, the UHV chamber has a base pressure below $3x10^{-10}$ torr. For surface science analysis, the chamber is equipped with a cylinder mirror analyzer for Auger electron spectroscopy and a quadrupole mass spectrometer for residual gas analysis and temperature

programmed desorption (TPD). An ion gun is used to sputter the sample for cleaning. Gasses are introduced to the chamber through various leak valves. The chamber is equipped with a sample manipulator with x, y, z, θ, and tilt. Included on the manipulator are ¼ inch hollow copper feedthroughs to deliver electrical power for resistive heating and are filled with LN_2 for cooling. Copper braids are used to connect the end of the feedthroughs to the UHV docking mount located at the end of the manipulator shaft. Type K thermocouple feedthroughs are also attached on the manipulator and interconnected to the UHV docking mount by 0.01 inch thermocouple wires.

II. Sample Mount

The sample mount consists of a stainless steel backing, 2 ceramic pieces, 2 L-shaped copper posts, 2 stainless steel posts and 2 L-shaped chromial and alumial pins (type K thermocouple) assembled as shown in figure 4.6. The stainless steel backing is a ½ inch thick, 1 inch diameter cylinder with a square hole cut in the back to attach to a standard ½ inch ratchet head. A 3/16 inch diameter locking pin that is 1/8 inch long is welded to the side 1/8 inch from the back. 4 each of 0-80 and 0-64 tapped holes are made on the outer edge of the front side of the steel backing to attach ceramic pieces. The first ceramic piece is used to separate the power pins for resistive heating from the backing, in essence acting as an electro-break. The ceramic piece is a ¼ inch thick Macor disk which is held to the steel

backing by 4 0-64 screws. In addition, there are 4 through-holes for 0-80 screws to hold the upper ceramic disk to the steel backing. 4 L-shaped pins are placed on top of the Macor electro-break. The L-shaped pins can be thought of as 2 unequal length cylindrical posts sitting on a thin rectangle bridge and held in place by screws. Two of the L-shaped pins are made of Glid-Cop (copper doped with 1.5% alumna for hardness at high temperatures) for electrical and thermal conduction and the other two pins are for type K thermocouple connections. The L-shaped pins are set 90 degrees to each other with the Glid-Cop pins set 180 degrees apart. The long side of the L-shaped pins are placed near the center with the short end near the edge of the Macor disk. The top ceramic piece is also ¼ inch thick with a ½ inch hole in the middle. 4 through holes ¼ inch wide and set 90 degrees apart were made near the outer edge. The piece fits over the pins with the long side of the pins sticking through the hole in the middle and short side sticking through the outer through holes. The top ceramic piece is also machined to inset the thin rectangle bridge so that the top and bottom ceramic pieces can sit flush with each other. The top ceramic piece is held to the stainless backing by the 0-80 screws. 4 holes ¼ inch diameter are made through the ceramic pieces and the stainless backing for conductance during gas recirculation and pumping. The long side of the Glid-Cop power pins are tapped at the end so that 2 stainless steel pins can be screwed in. The 2 stainless pins are the platform to which the sample is attached. A Pt(111) single crystal is spot welded on the back to 2 strips of 0.02 inch thick Pt foil. These strips are then spot welded to the stainless posts. This

way, the single crystal is protected from warping due to differences in expansion coefficients when the sample is heated. 0.01 inch K type thermocouple wires are spot welded to the back of the crystal and to their respective L-shaped pins.

III. UHV docking mount and transfer arm

The UHV docking mount (figure 4.7) connects to the end of the sample manipulator and provides electrical and thermocouple connections to the sample mount. The UHV docking mount can be broken up to 3 main components. The 1st component is the main housing. This is a stainless steel cylinder with hole cut in the center to fit the sample mount. A 3/16 inch groove 1 inch long is cut on the inside edge along the long axis of the cylinder. The groove then turns 90 degrees and a 60 degree arc of the same groove is cut. The purpose of the grooves are such that when the sample mount enters the docking mount, the sample mount locking pin slides in the groove as it enters then rotating 60 degrees to hold the sample mount in place. The second component of the docking mount is the ceramic Macor disk capping the end of the stainless steel cylinder. This disk has a center hole to allow only the sample to pass through. In addition, the Macor disk houses 4 spring loaded pins which connects to the sample mount to transfer power and make thermocouple connections. A ½ inch diameter ¾ inch long pin is located on the bottom of the docking mount to hold the unit in place during transfer.

The sample mount is the mobile unit moving between the UHV docking mount and the high pressure reaction cell. This movement is carried out by a magnetically coupled transfer arm (MDC) with a ratchet head welded on the end. The ratchet head connects to the corresponding receptor at the end of the sample mount on the steel backing. The transfer arm is connected to the chamber via a 2-3/4 conflat with a bellows in between to allow for fine adjustment during transfer alignment. During sample transfer, the manipulator holing the docking mount moves down and the ½ inch diameter ¾ inch long pin at the bottom the docking mount fits in a hole on a rigid structure attached to the chamber. With the pin in the hole, the docking mount is held in place for the transfer arm to be pushed on and pulled off during transfer. As the sample mount enters the docking mount, its locking pin slides in the groove on the docking mount. As the sample mount hits the end of the groove it is rotated in the curved groove. During this rotation process the sample mount connecting pins push back the spring loaded pins on the docking mount to crate a contact.

IV. High pressure reaction cell

The high pressure cell is a 600ml stainless steel cell electroplated with gold to reduce reactivity (figure 4.8). The cell is connected to the UHV chamber through a 2-3/4 conflat and a gate valve. 2 CaF_2 windows with 2 inch clear aperture are mounted on 4-1/2 inch flanges for input and exit laser beams. A CaF_2 window on

the exit side was installed to allow the IR beam reflected from the crystal to travel out of the cell. This beam is used for gas phase normalization and phase measurements. The sample transfer system design is similar to the UHV docking mount except that the cylinder portion is built as the entrance of the cell and the ceramic disk with the spring loaded pins are on a removable flange inserted from the top of the cell (figure 4.9). One gate valve is sufficient to seal the reaction cell from the UHV chamber, however in order to detach the cell from the UHV chamber, two gate valves are necessary.

3 Popit valves are attached to the cell for gas input, recirculation, and pumping with a turbo molecular pump. A gas manifold system was used to introduce gases at high pressures and for evacuation. A gas chromatograph was connected to the recirculation loop for gas analysis. A turbo molecular pump was connected to evacuate the cell to UHV pressures prior to opening the gate valve connected to the main UHV chamber.

During an experiment, the gas composition inside the high pressure cell can be monitored by either the HP 6850 gas chromatograph with both flame ionization detection (FID) and thermal conductivity detection (TCD) through a ¼ inch packed column or by feeding the gas back to the main chamber through a leak valve. The leak valve is positioned such that the gas entering the chamber is only a few centimeters away from the ionizer of the quadrapole mass spectrometer.

The utility of the high pressure cell as a reactor is demonstrated in figures 4.9 and 4.10. These two figures show ethylene hydrogenation with 1 to 10 ethylene to hydrogen ratio on a Pt(111) crystal in the high pressure cell. In figure 4.10, the Pt(111) crystal was covered with carbon, as seen by the Auger spectrum and the corresponding reaction data gathered by a gas chromatograph showing very little activity after 2 hours. In contrast, figure 4.11 show the reaction taking place on a clean Pt(111) surface where by all the ethylene was converted to ethane after 75 minutes.

C. Programming Auger and mass spectrometer controls

The PHI 10-155 CMA and the UTI-100 mass spectrometer are both controlled by programs written in Labview. A National Instruments data acquisition board, ATMIO64-XE, was used for all A/D and D/A conversion. In the Auger program, the computer read inputs from the Auger control unit as well as the lock-in amplifier. Since the control unit did not allow computer control, the parameters for the Auger scan was preset on the control unit. For the mass spectrometer, a RGA program was written. This program allowed for a mass range and resolution to be selected as well as the acquisition time to spend at each mass. The mass spectrometer control unit accepted analog voltage input which had a correlation of 30mv per mass unit. Through this, the desired range can be scanned with the program stopping at each mass at the set resolution and would

collect the mass signal for a designed amount of time at a collection rate of 50kHz. The resulting mass spectrum would be plotted on the display screen as well as a running average of several selected masse. In addition to the RGA program, a 5 mass TPD program was written. This program collected data from the mass spectrometer at 5 fixed masses. In the TPD program the masses signal must be collected as a function of the temperature on the crystal. The Program scans through all five masses and collects the corresponding temperature before starting over. In this fashion, a ramp rate greater than 20K/sec can be used and still maintain good resolution of all five masses. On the front display, the real time mass signal is displayed along with the temperature on the crystal which is read by a thermocouple. After the scan, all five masses are plotted with their corresponding mass signal at specific temperatures. In the appendix, all three programs are presented with their from panels display as well as the wiring diagrams.

References

1. Y.R Shen, Nature **337**, 519, (1989).
2. T. G. Rucker, K. Franck, D. Colimb, M. A. Logan, and G. A. Somorjai, Rev. Sci. Instrum. **58**, 2292, (1987).
3. A. Ludviksson, J. Yoshihara, and C. T. Campbell, Rev. Sci. Instrum. **66**, 4370, (1995).
4. J. Szanyi and D. W. Goodman, Rev. Sci. Instrum. **64**, 2350, (1993).
5. Y. N. Wang, R. McAllister, R. G. Sherman, G. W. Simmons, and K. Klier, Rev. Sci. Instrum., **63**, 5767, (1992).
6. R. A. Campbell and D. W. Goodman, Rev. Sci. Instrum., **63**, 172, (1992).
7. T. A. Jachimowski, J. Lauterbach, Rev. Sci. Instrum., 69, 2757,(1998).
8. Zhang, J. Y.; Huang, J. Y.; Shen, Y. R. *Optical Parametric Generation and Amplification*, 1st ed.; Harwood Academic Publishers: Luxembourg, 1995; Vol. 19.

figure 4.1 for laser

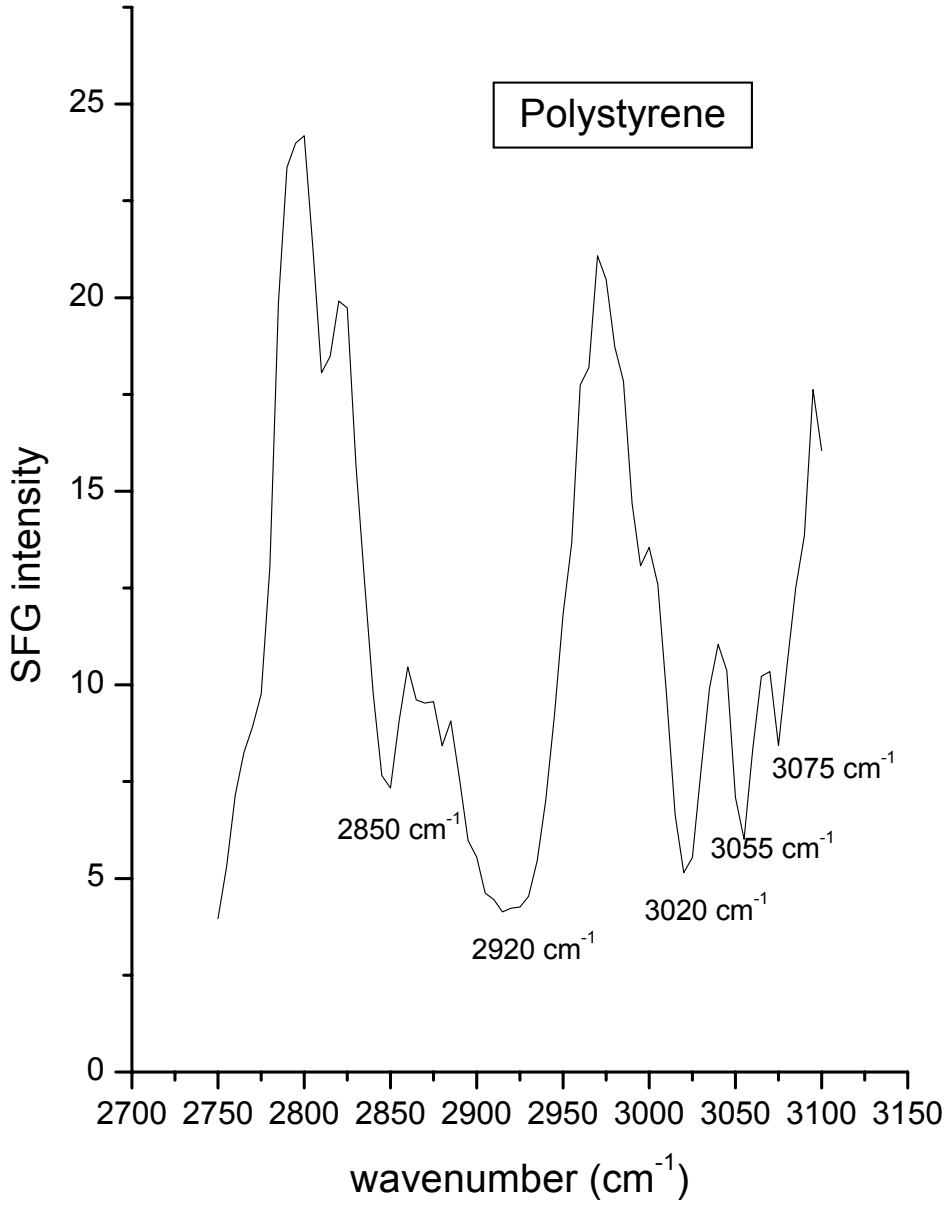

Figure 4.2 Infrared transmission spectrum of polystyrene from the $LiNbO_3$ syatem.

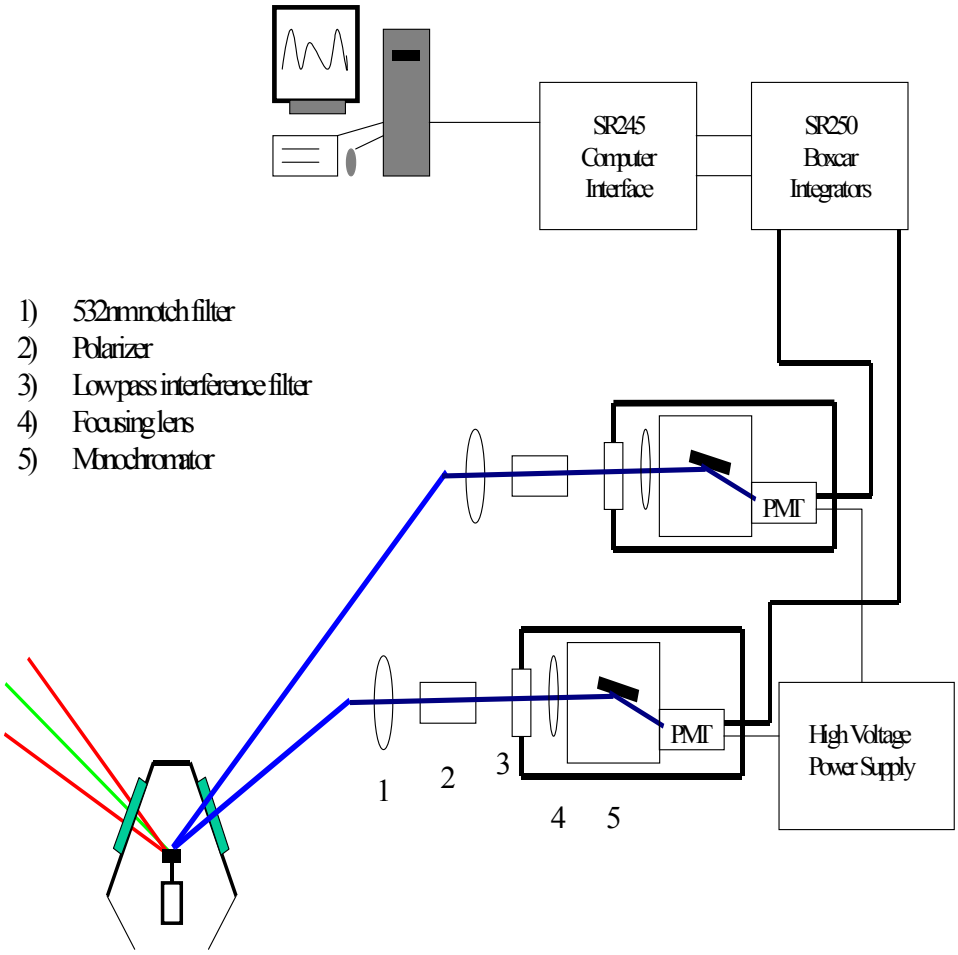

Figure 4.3 Detection system for 2-IR 1-visible SFG experiments, for experiments where only 1 IR is used, only 1 detection setup is needed.

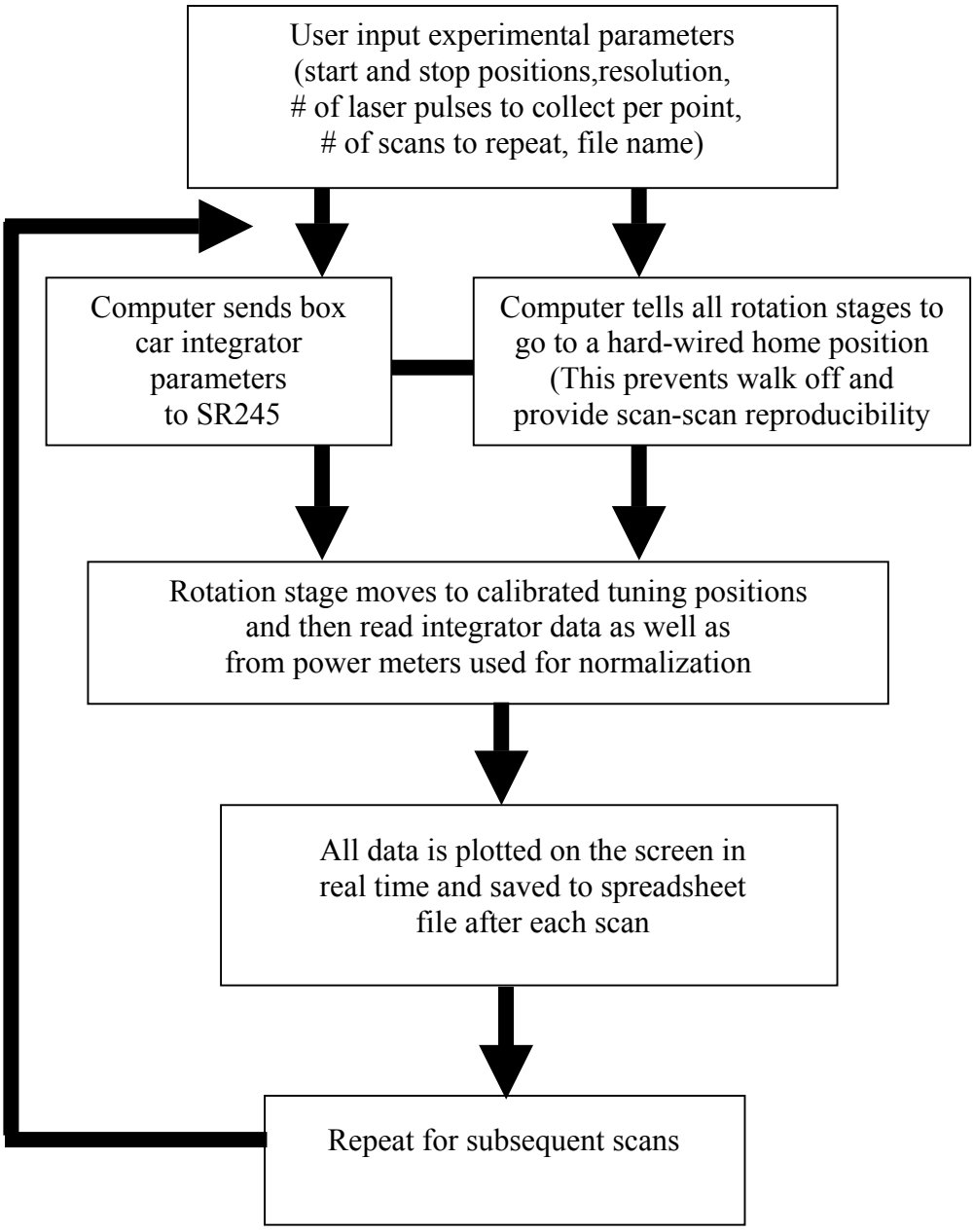

Figure 4.4 Programming flowchart for tuning the OPA/OPG laser system and collect data from the boxcar integrators.

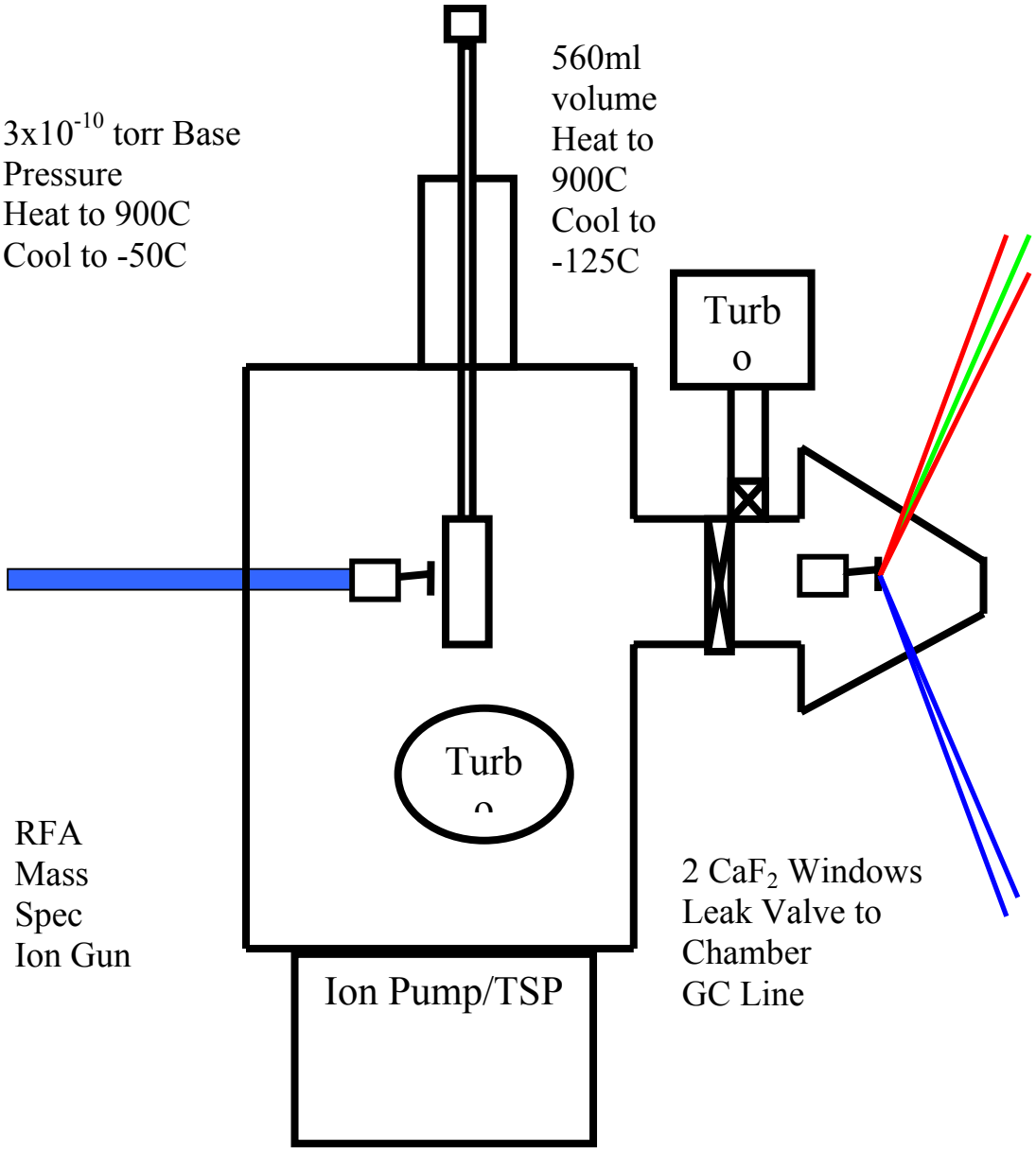

Figure 4.5 UHV high-pressure reaction system with transfer system

Figure 4.6 for sample mount

figure 4.7uhv docking mount

figure 4.8 high pressure cell

figure 4.9 high pressure docking flange

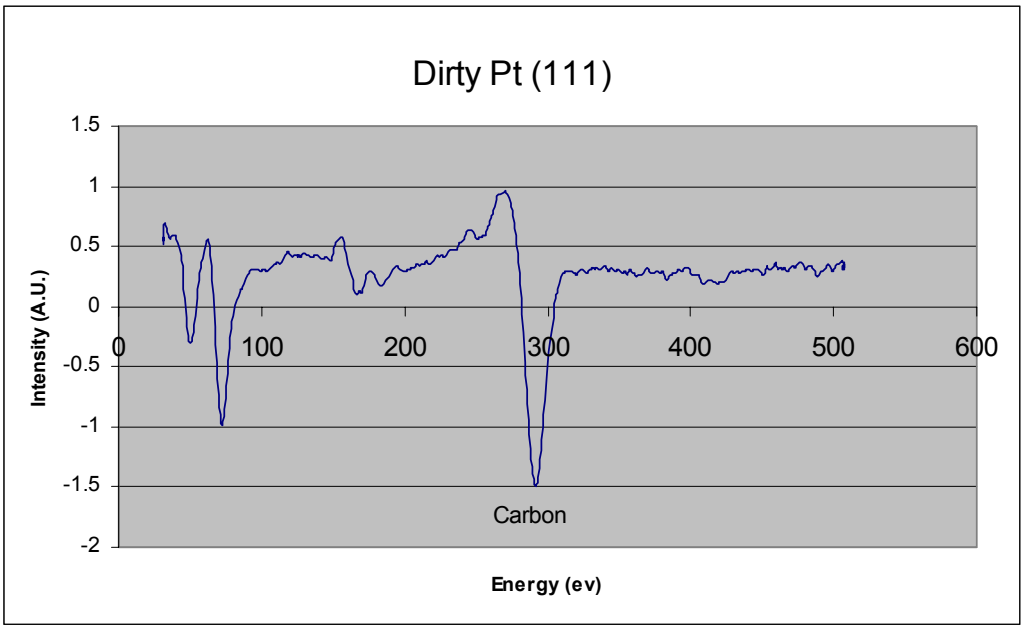

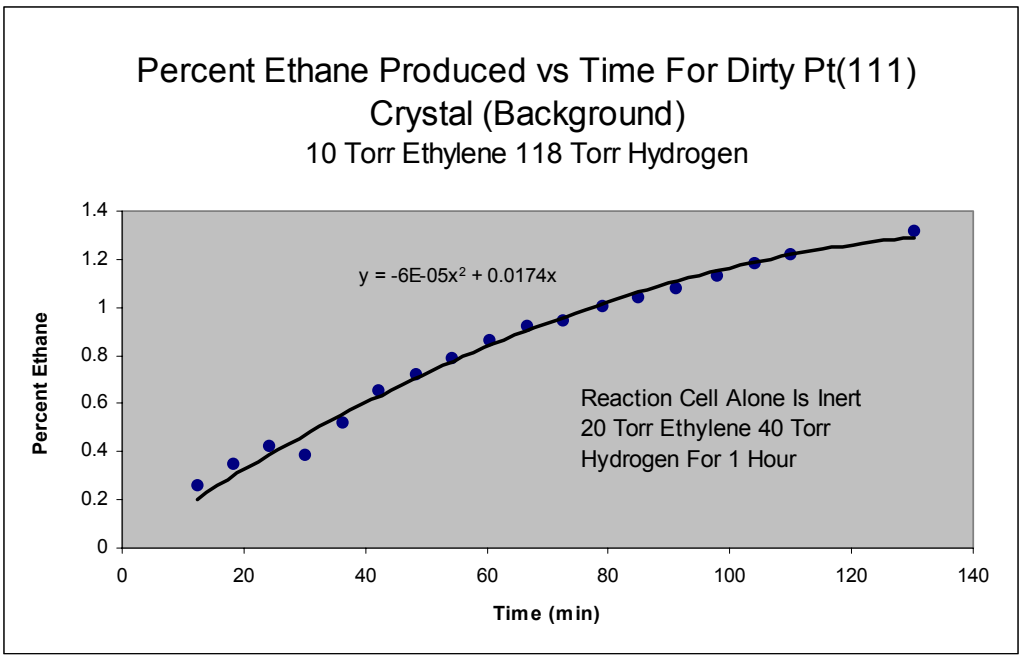

Figure 4.10 Ethylene hydrogenation in the high pressure cell on a dirty crystal with virtually no reactivity.

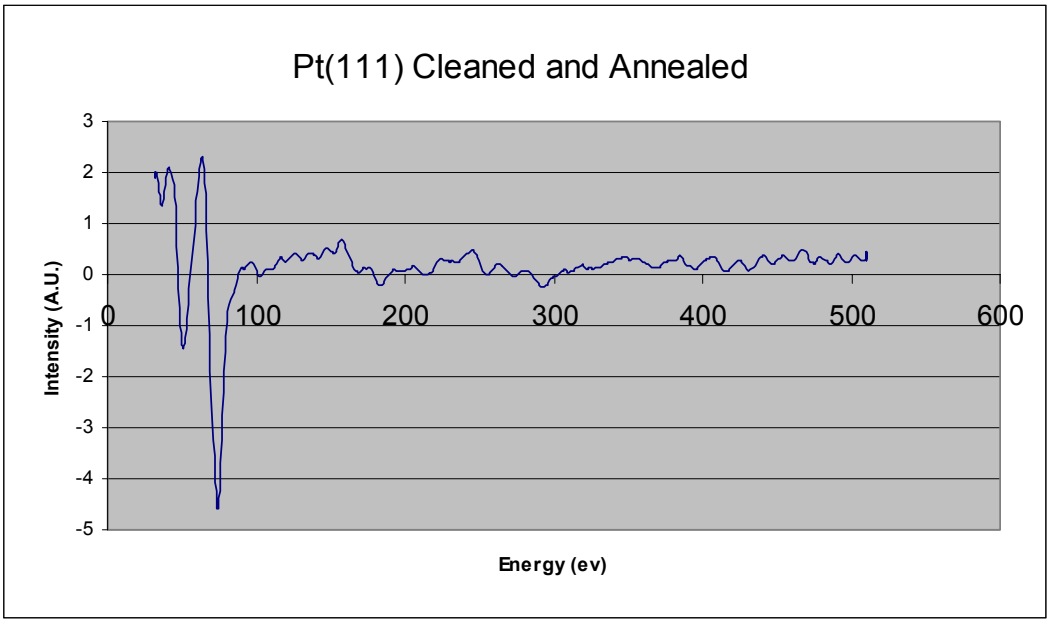

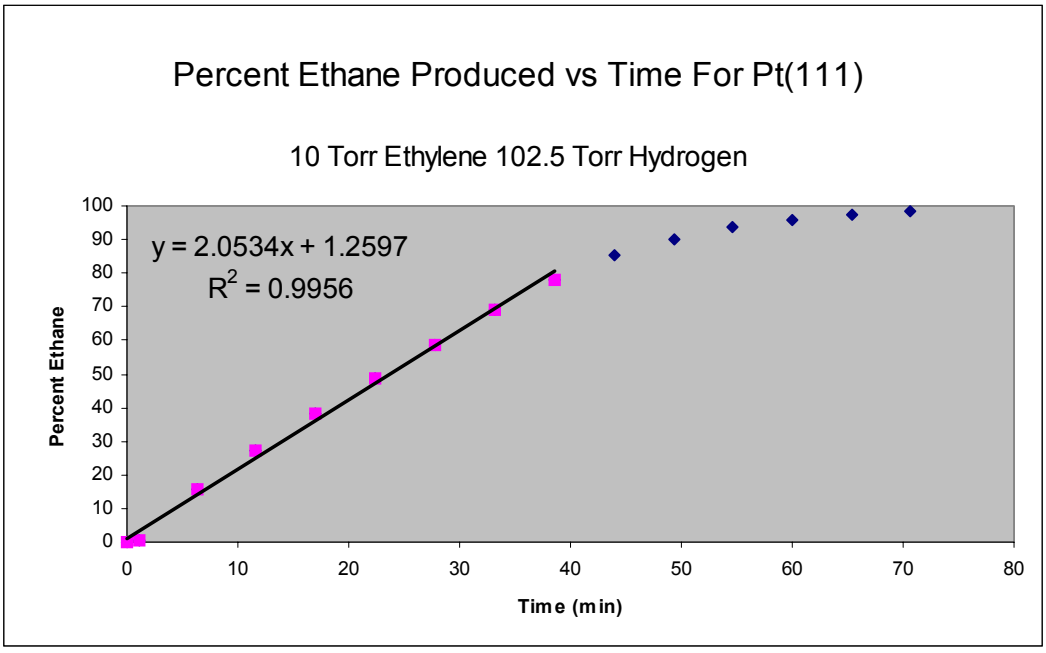

Figure 4.11 Ethylene hydrogenation in the high pressure cell on a clean crystal showing total conversion after 75 minutes.

Chapter 5

High pressure high temperature CO adsorption on Pt(111)

Does carbon monoxide dissociate on platinum surfaces? It is generally believed that CO can dissociate on Ru, Fe, and Ni but not on Pt[1]. However there exists a report showing x-ray photoelectron spectroscopy (XPS) evidence that CO adsorbed on platinum surfaces with high Miller indices does dissociate[2]. Such crystalline surfaces have high concentrations of step and kink sites in addition to terrace sites. The carbon 1S XPS spectrum exhibits a chemical shift indicating that CO dissociates at kink sites which are then blocked by adsorbed carbon product atoms. There was no evidence of CO dissociation at step and terrace sites at low CO pressures. Thermal desorption of CO from the Pt(111) has shown that CO adsorbed on Pt(111) at low pressures (~10^{-7} Torr) desorbs intact[3]. At step and kink sites, the adsorbed CO has higher heat of adsorption, suggesting stronger binding of CO to these defects and consequently weakening of the C=O bond. This is well correlated with the results of vibrational spectroscopic studies showing that the stretch frequency of atop CO decreases from 2095 cm^{-1} for atop CO on Pt(111) to 2055-2065 cm^{-1} for CO adsorbed at kink and step sites[4-6]. With the weaker CO bond, it is then possible that CO may dissociate at defect sites on platinum surfaces.

As an in-situ surface-specific technique, sum-frequency generation (SFG) vibrational spectroscopy can be used to study CO on transition metals at high pressures and temperatures. We are interested in how CO on Pt(111) behaves under such conditions. We report here SFG and Auger spectroscopy measurements that show evidence of CO dissociation on Pt(111) at high CO pressure (P_{CO} = 400 Torr) and high temperature (673K). SFG spectra of the CO stretch mode at various temperatures suggest that surface modification may have occurred with possible formation of carbonyl-like species at sufficiently high temperatures. After heating the sample under high CO pressure to 673K, the spectra displayed irreversible changes. Upon evacuation of the sample chamber, Auger spectroscopy detected the presence of carbon on the surface. These findings indicate that the Boudouard reaction, $2CO \rightarrow C + CO_2$, presumably catalyzed by the formation of carbonyl complexes, can occur on Pt(111) at high CO pressure and high substrate temperature.

The experimental arrangement has been described elsewhere[7]. For SFG spectroscopy, the tunable infrared radiation between 1500 cm^{-1} to 2400 cm^{-1} was generated from a 20 ps, 20 Hz Nd:YAG laser through optical parametric processes. It was overlapped spatially and temporally with the 532 nm beam from the laser at the Pt(111) surface with spot diameters of 0.5 and 2 mm, and incident angles of 60^0 and 55^0 respectively. The 532 nm and infrared beams were both p-polarized and their pulse energies at the surface were 250 μJ and 60 μJ respectively. For sample preparation, an ultrahigh vacuum-high pressure (UHV-

HP) system with a base pressure less than $3x10^{-10}$ Torr was used. It allowed us to clean and characterize the Pt(111) crystal in UHV and later transfer it under UHV to the high-pressure reaction cell for SFG measurements. The Pt(111) crystal was cleaned by cycles of Ar^+ sputtering (12 minutes at $3x10^{-5}$ Torr Ar, 1000V, 20mA emission current), heating in O_2 ($5x10^{-7}$ Torr O_2 from 300K to 1123K then 2 minutes at 1123K) , and annealing (1 minute at 1133K at below $2x10^{-9}$ Torr). Detailed description of the UHV-HP system and cleaning procedures has also been described elsewhere[8]. Auger electron spectroscopy was used to check cleanliness of the surface. After the last cycle of cleaning and annealing, the Pt(111) crystal was exposed to $1x10^{-7}$ Torr of CO. The sample was then transferred to the high-pressure reaction cell and SFG spectra were collected at room temperature at $1x10^{-7}$ Torr constant CO pressure. Since SFG is a second order nonlinear optical process, its intensity depends on the laser condition. To account for this fluctuation, the intensity of the atop CO peaks was used for day to day normalization. The overall intensity fluctuation is less than 10%. When compared to the published works[7,9-11], we confirm the presence of CO on atop terrace sites. For each SFG measurement, at each wavelength, we simultaneously recorded the SFG signal and the intensities of the reflected infrared beam from the entrance window and the infrared beam reflected by the sample. The infrared intensity on the sample surface was then calculated by Beer's law assuming equal optical path for incident and reflected infrared beams inside the high-pressure cell. These measurements were needed to correct for laser fluctuations and for gas

phase absorption in the high-pressure reaction cell. By normalizing the infrared input on the sample and minimizing the cell path length for gas phase absorption, we have been able to detect the CO atop terrace site at 2095 cm^{-1} at 400 Torr CO pressure that was missed in previous studies (figure 5.1)[9].

The sum frequency signal intensity I_{SFG}, under the electric-dipole approximation[12], is proportional to the square of the second order nonlinear surface susceptibility $\chi^{(2)}$: $I_{SFG} \propto |\chi^{(2)}|^2$. The observed SFG spectra could be fitted to the resonant term of $\chi^{(2)}$

$$\chi^{(2)} = A_{NR} + \frac{A_R}{(\omega - \omega_0 - i\gamma)} \qquad (1)$$

where A_{NR} is the non-resonant contribution, ω_0 is the resonant vibrational frequency and γ is the line width and A_R is the resonant strength which is proportional to the product of the number of molecules on the surface, and the infrared and Raman transition moments. Therefore, the SFG spectra can be used to determine the surface coverage by fitting the A_R coefficient using equation (1).

Spectra covering the CO stretching frequency range from 1900 cm^{-1} to 2200 cm^{-1} were collected at variable temperatures with 400 Torr of CO pressure, and as a function of time at 673K and 400 Torr CO pressure. CO at bridge sites (~1800 cm^{-1}) was too weak to be observed under these experimental conditions.

Figure 5.2 shows the stretch vibrational spectra of CO adsorbed on the Pt(111) crystal at 400 Torr as the sample temperature was increased from 300K to 823 K. Each spectrum was obtained from the sum of three consecutive scans at constant temperature lasted for approximately 20 minutes total. At 823K, the SFG spectral features due to CO are no longer detectable. After heating at 823K for twenty minutes, the sample was cooled to room temperature under 400 Torr of CO pressure. Figure 5.3 displays the SFG spectra during the cooling process. The resonant CO feature reappears at 623K but clearly has a different strength compared to that observed in heating. The hysteresis behavior can be clearly seen in figure 5.4 which depicts the peak position versus temperature for both heating and cooling. Upon heating from 273 to 623K (the filled circles), the peak shifts to lower frequency. At 673K (the unfilled circles), the spectrum begins to vary with time. The CO peak becomes weaker and broader and keeps shifting to lower frequency until it reaches ~ 2040 cm^{-1} and disappears into background. The time evolution of the CO spectrum is shown in figure 5.5. Upon cooling, the CO peak recovers and shifts back to ~2077 cm^{-1} at 300K. Further heating and cooling no longer have any appreciable effect on the spectrum for a given temperature; the spectrum appears the same as that obtained in the last cooling process.

At the end of each experiment, the high-pressure cell was pumped out and the sample was transferred to the UHV chamber for Auger electron spectroscopy measurement. Figure 5.6 shows the Auger electron spectra after heating to two different temperatures under 400 Torr of CO. The presence of carbon on the

surface is evident by the 273 eV peak in the spectrum (Figure 5.6A) taken after heating the Pt(111) crystal at 673 K for 1 hour. This is in contrast to the absence of carbon on both the clean Pt(111) crystal and after heating the sample in 400 Torr of CO at 473 K for 1 hour (Figure 5.6B).

The vibrational spectra of CO adsorbed on Pt(111) surface in UHV have been widely studied by infrared reflection absorption spectroscopy (IRAS)[4,13-16]. It is known that at saturated coverage, atop CO on the terrace sites exhibits a stretching frequency at 2095 cm^{-1}, which shifts to lower frequency as the coverage decreases due to the reduction of dynamic dipole-dipole coupling[15,16]. The existence of strong dynamic dipole-dipole coupling complicates the interpretations of vibrational spectra. Substrate temperature also plays an important role in determining the resonant frequency. IRAS experiments in UHV have shown that the CO vibrational frequency shifted to lower frequency when the substrate temperature was increased from 50K to 300K[17]. This frequency shift was attributed to anharmonic coupling to the frustrated translation mode.

CO adsorption on platinum surfaces under high CO pressure and at room temperature has been investigated by SFG technique in previous experiments by our group.[7,9]. The spectra showed a decreasing atop CO peak superimposed on a broad shoulder with increasing pressure. In this current study, we have observed, in contrast, the presence of the atop CO SFG peak at 400 Torr. The discrepancy is mainly due to gas phase CO absorption which is reduced in this study by using shorter optical path length in the high-pressure cell and proper normalization

scheme. The broad shoulder around 2000-2040 cm^{-1} was suggested[9,18] to be associated with the formation of carbonyl binary complexes on platinum surface under high CO pressure

We now consider the results presented in Figures 5.2 through 5.4 in some more detail. If we start with a clean Pt(111) surface, the CO spectrum changing with substrate temperature was always reversible and no trace of carbon on the surface was found as long as the temperature was lower than 623K. In this temperature region, the CO coverage did not change by more than 10% as judged from the deduced A_R value from fitting the spectra. Since the surface CO concentration remains roughly the same over this temperature region, the frequency shift with temperature can not be due to coupling between CO molecules. One would think it could be due to surface roughening, as under high CO pressure, the Pt(111) surface may get roughened with increase of temperature. This would result in an increase of CO adsorbed on step and kink sites leading to the CO peak shift toward lower frequency. To check this possibility, we studied CO adsorption on a sputtered Pt(111) surface (15 minutes at $3x10^{-5}$ Torr Ar, and 1KV energy) at room temperature (figure 5.7) . At 10^{-7} Torr of constant CO pressure, the atop CO peak appeared at 2085 cm^{-1} with a width (γ) of 14 cm^{-1}. For comparison, CO on the annealed surface appears at 2095 cm^{-1} with a 7 cm^{-1} peak width. However, when the CO pressure was increased to 400 Torr, the CO peak position moved back to 2093 cm^{-1} and the peak width sharpened to about 8 cm^{-1}, closely resembling that of an annealed surface. Upon evacuation of CO, the peak

position remained at 2095 cm^{-1}. This striking result indicates that defects created by argon sputtering can be annealed out by high pressure CO, and surface roughening does not appear to be the reason for the temperature dependent frequency shift in the 295-627 K region. The most likely explanation for the frequency shift is through the effect of anharmonic coupling[17] to the lower frequency CO-Pt modes which increases with temperature resulting in a decrease of the CO stretch frequency.

At 673K, the CO vibrational spectrum appears to vary with time (Figure 5.5). The CO peak decreases in intensity, shifts from 2070 to 2040 cm^{-1}, and broadens from 10 to 60 cm^{-1}. It finally disappears beyond our detection limit after one hour heating at 673 K. Auger spectrum taken afterwards gives evidence of the presence of carbon on surface. These results indicate that at this temperature, the equilibrium CO coverage must have been reduced with time by thermal desorption and the surface may have been modified. Some CO must have dissociated to yield carbon left on surface. The frequency shifted, broadened peak suggested that CO now adsorbs on a modified Pt(111) surface. The peak position suggests that CO may have formed carbonyl binary complexes with platinum on surface. Eventually, at this temperature, all adsorbed CO must either desorbed from or dissociate on the surface. It has been shown that CO can dissociate at kink sites of the platinum surface. This would happen more readily if the platinum surface is modified or roughened at high temperature. It is possible that the transport of the platinum surface atoms, which results in surface roughening at

high temperatures, is catalyzed by the formation of metal carbonyl species which could also facilitate CO dissociation via the exothermic Boudouard reaction $2CO \rightarrow C + CO_2$.

After heating at 673K for more than one hour, if the platinum sample was cooled under the same CO pressure (400 Torr), the CO spectrum reappeared as a strong narrow peak with a strength A_R corresponding to roughly saturation coverage of CO. However, the peak position was downshifted by ~20 cm^{-1} from the one obtained at the same temperature before the sample was heated to 673K. This is described in Figure 5.4. As we mentioned earlier, the modified or roughened platinum surface should have been annealed after being exposed to high CO pressure. Therefore, the downshift of the peak is not due to surface modification or roughening, but is believed to result from CO co-adsorbed with carbon on the surface, the temperature variation of the spectrum was again reversible in the range of 300-630K.

It is interesting to note that high CO pressure can cause platinum surface modification at all temperatures. At low temperature it appears to help order a roughened platinum surface. At high temperature it seem to cause roughening of the surface that leads to CO dissociation. Platinum is an excellent catalyst for CO oxidation. It is likely that CO dissociation that leads to carbon deposition on the surface can provide an important reaction channel to combustion to CO_2 in addition to the direct oxidation of molecular CO by atomic oxygen. Thus the

onset of the Boudouard reaction $2CO \rightarrow C + CO_2$ could play an important role in the ignition of CO combustion that makes the process self-sustaining.

It needs to be pointed out that the gas phase molecules do not contribute to the SFG signal which is generated solely from the adsorbed species at interfaces that have no center of inversion. However, the gas phase molecules absorb infrared radiation that attenuates the infrared intensity at the sample. If the gas phase absorption peaks overlap with the SFG signal, it will lead to erroneous spectral assignments. Thus, recent effort in our laboratory to use smaller volume cells to reduce the gas phase absorption and proper normalization scheme has led to higher intensity SFG spectra that could be detected at higher pressure. The disappearance of atop CO peak and other features in our previous high pressure CO spectra[7,9] was due to the gas phase absorption. We are currently investigating gas phase absorption for the alkene systems[19-22] at high pressure

In conclusion, at high CO pressure (400 Torr), CO dissociation on Pt(111) surface has been observed at 673K. At these conditions, Pt(111) surface may be roughened which results in the formation of lower coordination sites such as kink and adatom sites which can facilitate CO dissociation. Mechanism of roughening is most likely through carbonyl formation. The formation of this carbon may provide an alternative reaction mechanism for CO oxidation which could play an important role in the ignition of CO oxidation reaction.

References

[1] G.A. Somorjai. *Introduction to Surface Chemistry and Catalysis* 442-595 (John Wiley &Sons, NewYork, 1994).

[2] Y, Iwasawa, R. Mason, M. Textor, G.A. Somorjai, Chem. Phys. Lett. 44, (1976) 468.

[3] G Ertl, M. Neumann, and K.M. Streit, Surf. Sci. 64 (1977) 393.

[4] B.E. Hayden and A.M. Bradshaw, Surf. Sci. 125 (1983) 787.

[5] B.E. Hayden, K. Kretzschmar, A.M. Bradshaw, and R.G. Greenler, Surf. Sci. 149 (1985) 394.

[6] R.K. Brandt, R.S. Sorbello, and R.G. Greenler, Surf. Sci. 271 (1992) 605.

[7] X. Su, P.S. Cremer, Y.R. Shen, and G.A. Somorjai, J. Am. Chem. Soc. 119 (1997) 3994.

[8] K. Kung, P. Chen, F. Wei, Y.R. Shen and G.A. Somorjai, to be published.

[9] X. Su, P.S. Cremer, Y.R. Shen, and G.A. Somorjai, Phys. Rev. Lett. 77 (1996) 3858.

[10] C. Klunker, M. Balden, S.Lehwald, and W. Daum, Surf. Sci. 360 (1996) 104.

[11] H. Harle, K. Mendel, U. Metka, H.-R. Volpp, L. Willms and J. Wolfrum, Chem. Phys. Lett. 279 (1997) 275.

[12] Y.R. Shen, Nature 337 (1989) 519.

[13] R.A. Shigeishi and D.A. King, Surf. Sci. 58 (1976) 379.

[14] E. Schweizer, B.N.J. Persson, M. Tushaus, D Hoge, and A.M. Bradshaw, Surf. Sci. 213 (1989) 49.

[15] A. Crossley and D.A. King, Surf. Sci. 68 (1977) 528.

[16] C.W. Olsen and R.I. Masel, Surf. Sci. 201 (1988) 444.

[17] B.N.J. Persson and R. Ryberg, Phys. Rev. B 32 (1985) 3586.

[18] H. Harle, U. Metka, H.-R. Volpp and J. Wolfrum, Phys. Chem. Chem. Phys. 1 (1999) 5059.

[19] P.S. Cremer, X.C. Su, Y.R. Shen, G.A. Somorjai, J. Phys. Chem. B 101 (1997) 6474.

[20] P.S. Cremer, X.C. Su, Y.R. Shen, G.A. Somorjai, J. Phys. Chem. 100 (1996) 16302.

[21] P.S. Cremer, X.C. Su, Y.R. Shen, G.A. Somorjai, J. Am. Chem. Soc. 117 (1996) 2942.

[22] X.C. Su, Y.R. Shen, G.A. Somorjai, Chem. Phys. Lett.280 (1997) 302.

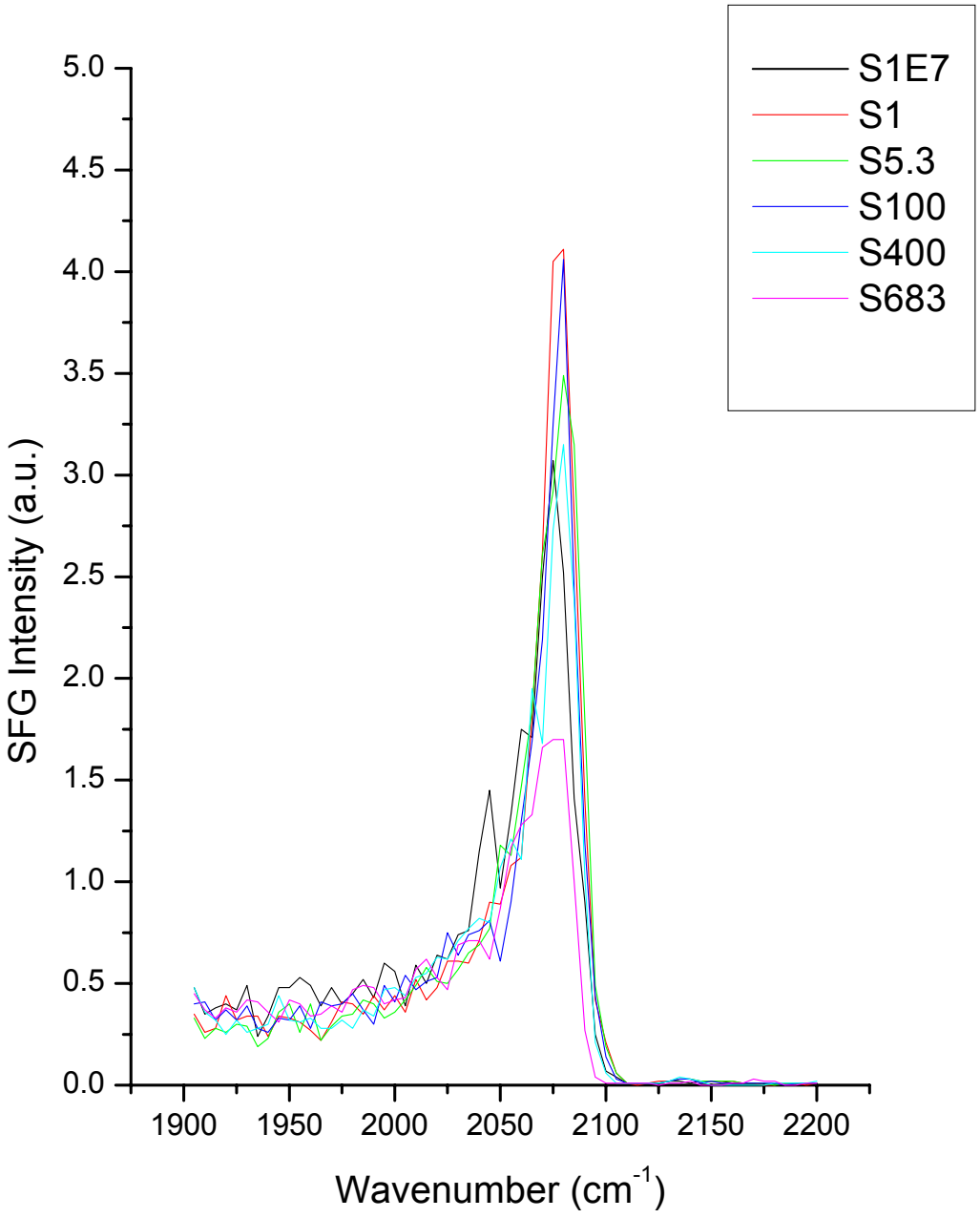

Figure 5.1 CO on Pt(111) from 10^{-7} torr to 683 torr at room temperature.

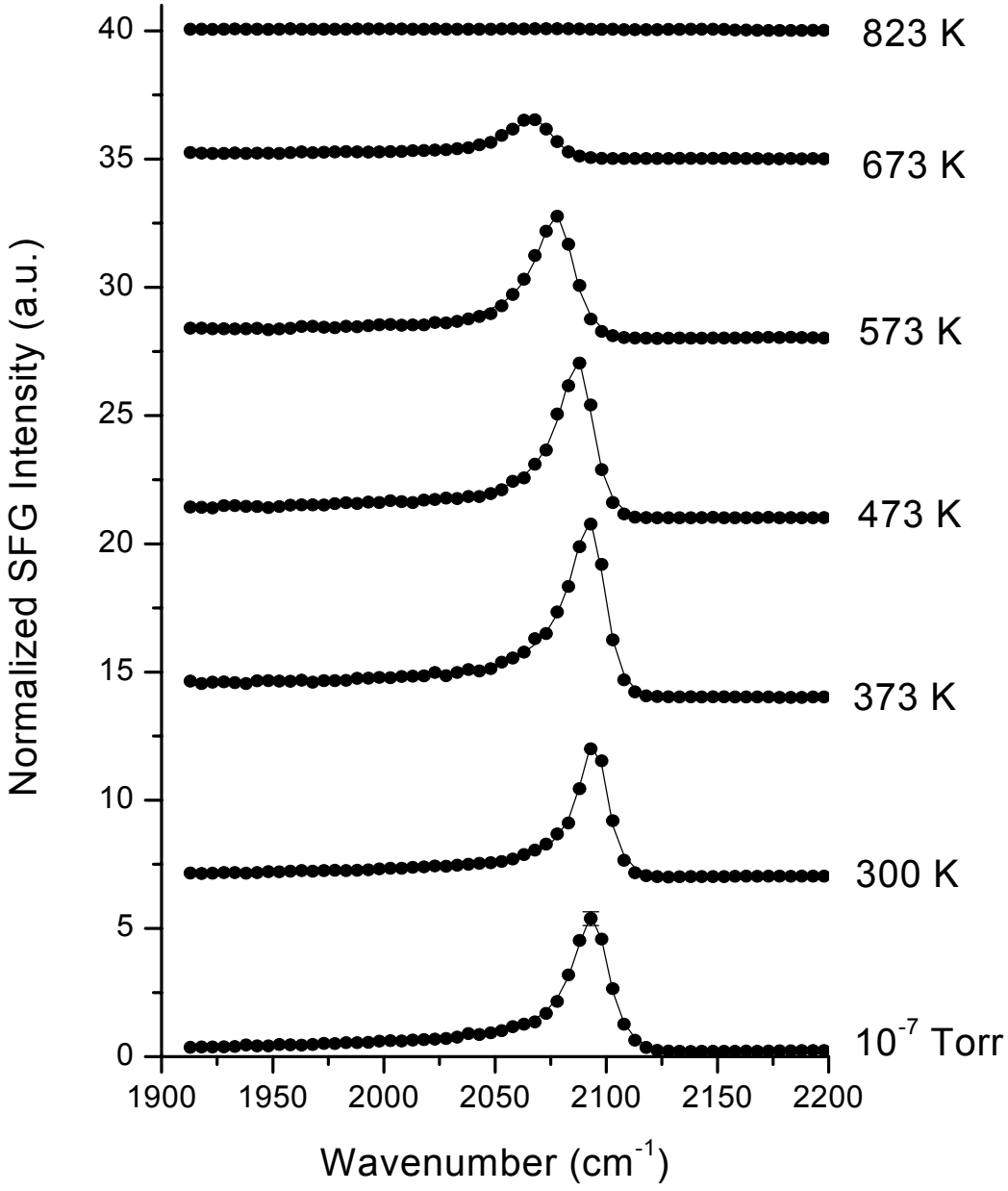

Figure 5.2 The SFG spectra of 400 Torr of CO on Pt(111) surface at various temperature during heating cycle. Solid lines are the fitted curves using equation (1).

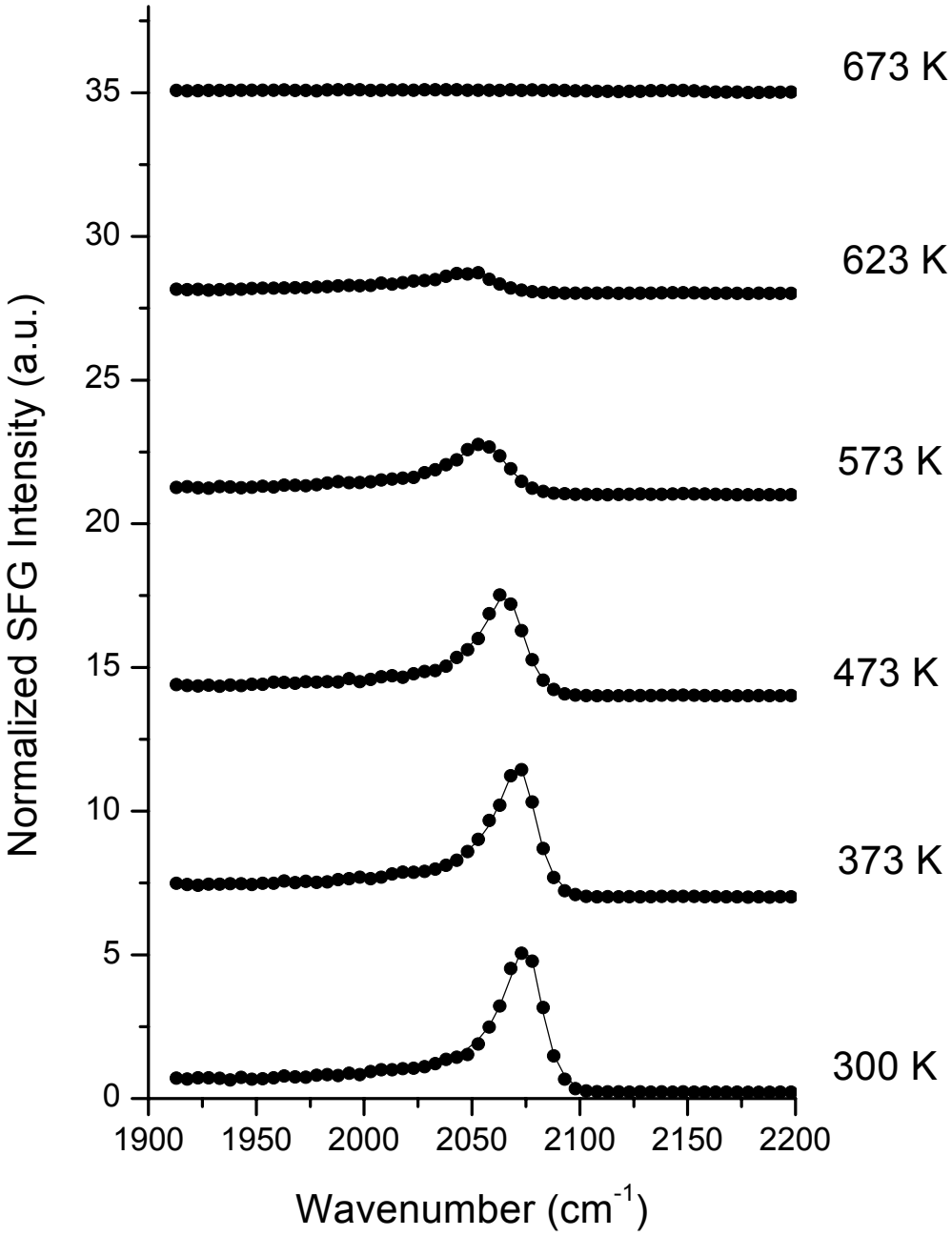

Figure 5.3 The SFG spectra for the cooling cycle. Solid lines are the fitted curves using equation (1).

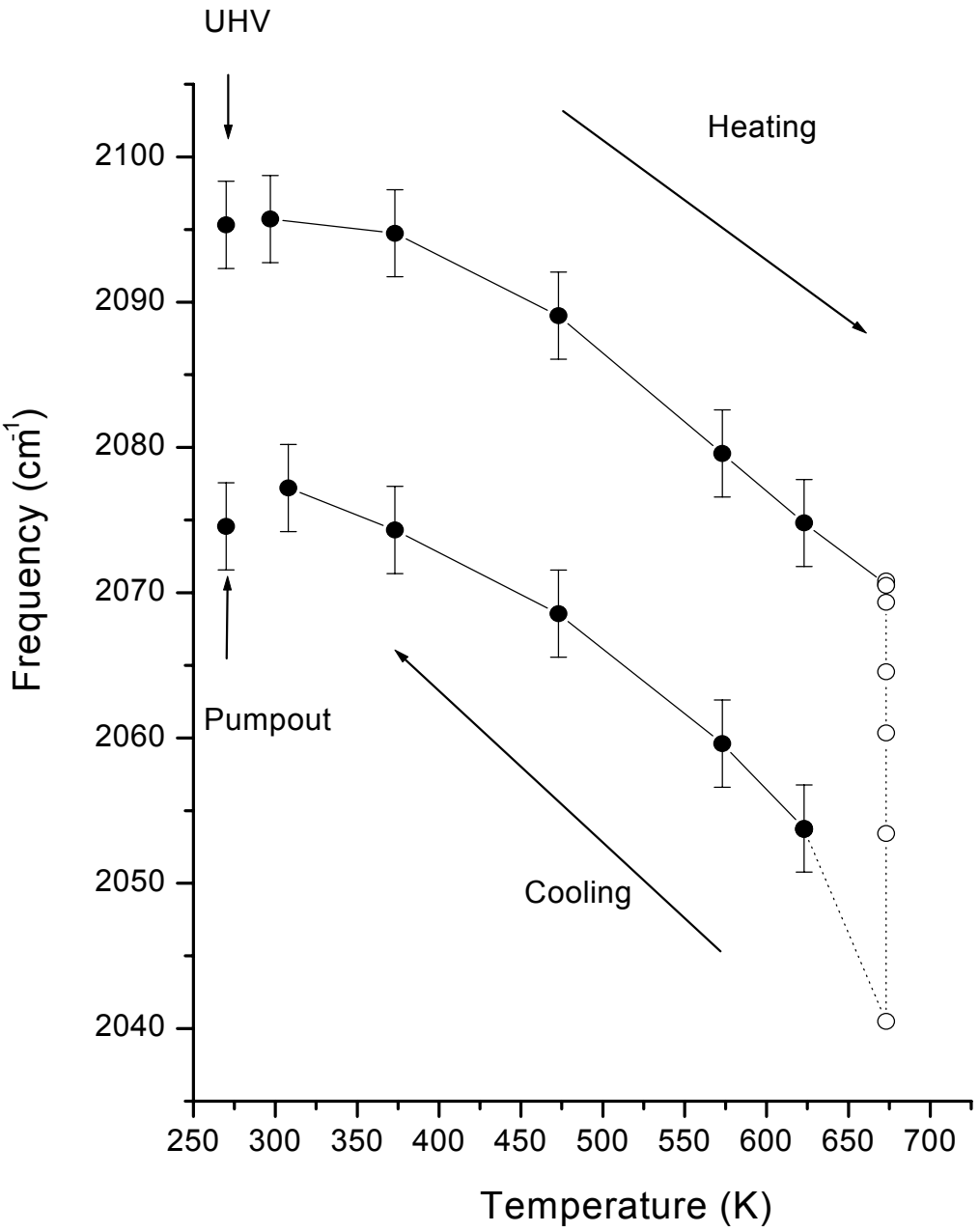

Figure 5.4 The CO vibrational frequency as a function of temperature. UHV indicates the peak position for 10^{-7} Torr of CO. The filled circles show the peak shift during heating and cooling processes. The open circles represent the peak position evolution at 673K. Hysteresis can be clearly seen in this figure, which is due to carbon formation at high temperature. After exposed to high pressure CO, the cell was evacuated to $2x10^{-9}$ Torr and its peak position is marked as pumpout.

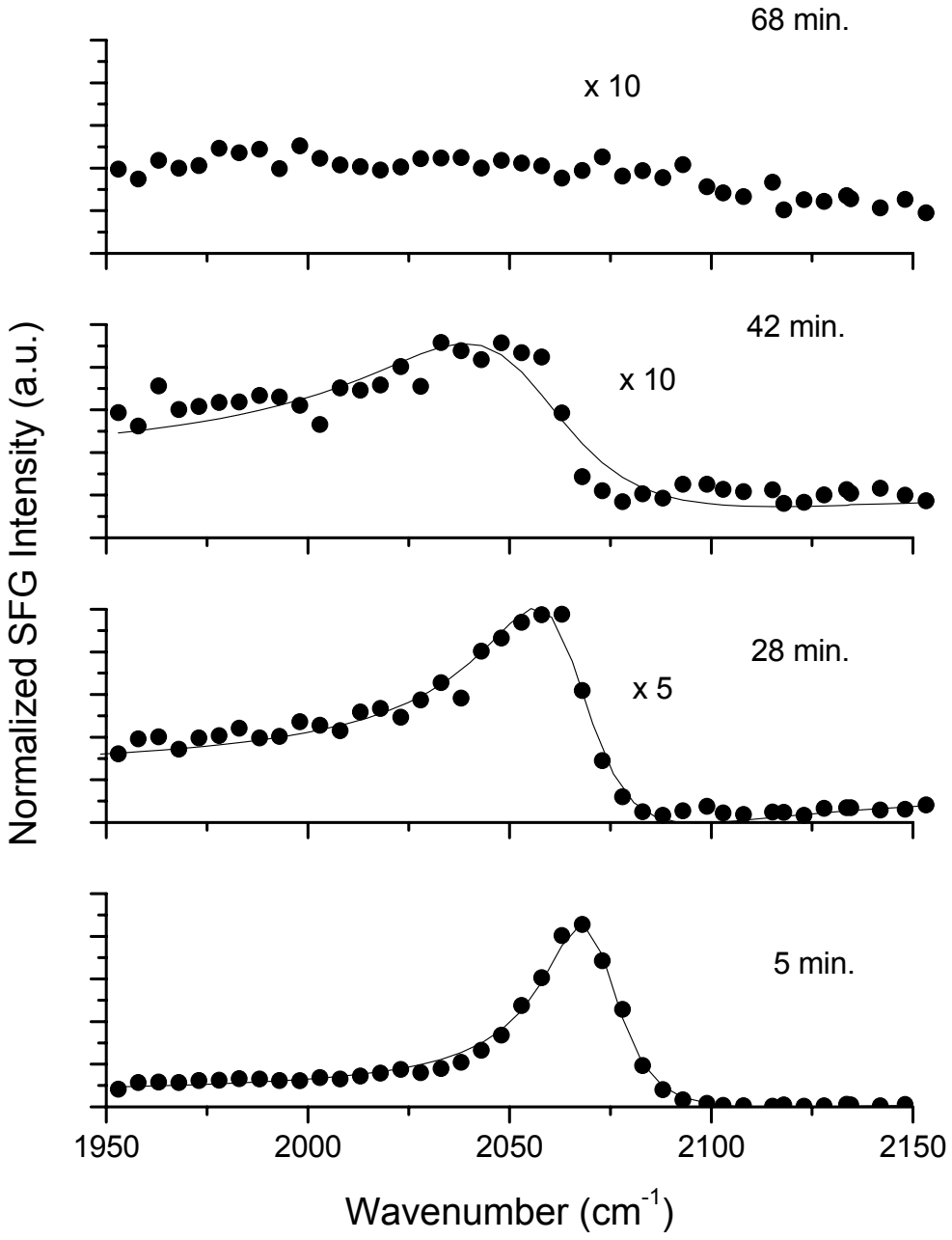

Figure 5.5 Time evolution of high-pressure CO SFG Spectra at 673 K.

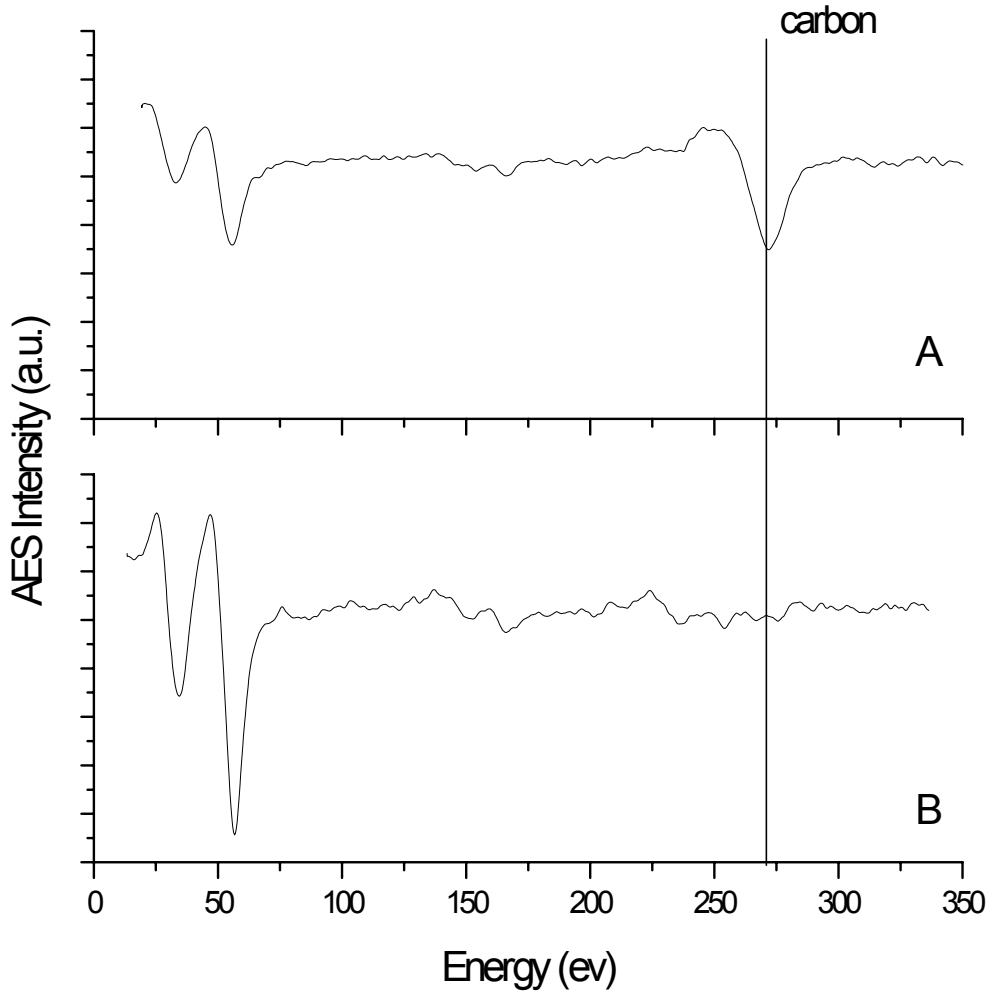

Figure 5.6 The Auger electron spectra for Pt(111) surface. A) After exposed to 400 Torr of CO at 673 K for one hour; B) After exposed to 400 Torr of CO at 473 K for one hour.

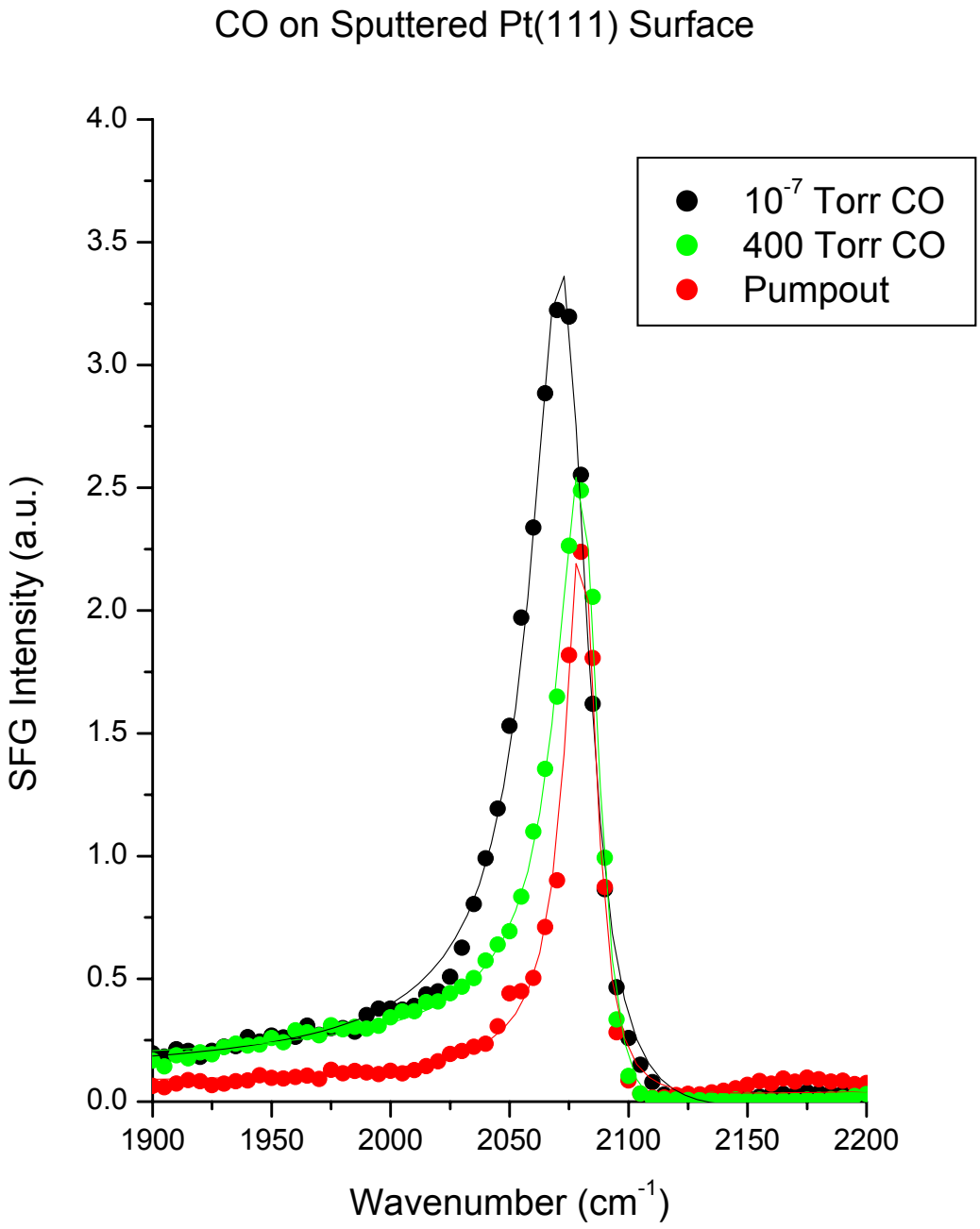

Figure 5.7 CO adsorption on a sputtered surface at room temperature

Chapter 6

CO coadsorption with ethylene and propylene on Pt(111)

The adsorption of CO, ethylene and propylene on Pt(111) have been some of the most studies systems in surface science. Due to the interesting nature of coadsorption ordering of either CO and ethylene and CO and propylene, these coadsorption systems have been studies by LEED. Work function measurements on Pt(111) indicate that CO is a electron acceptor while olefins like ethylene and propylene are electron donors. Since the coadsorbates can affect each other electronically through charge transfer as well as sterically, this seemly simple system is actually quite complected. Adding to the complexity is the whether pressure and temperature affect the ordering and orientation of these species.

The study of coadsorption system also leads to the understanding of promoters and poisons in catalytic reactions. Since real world catalytic reactions occur in environments where exact control of surface contamination are not possible, the role of how strongly adsorbed background gasses effect reaction are of great importance. In the case of ethylene hydrogenation on Pt(111), CO poisoning has been know in the literature for extended period of time. To run this catalytic reaction successfully, the order to which gases were introduced to the platinum surface affected its turnover. Experiments were often conducted where

hydrogen was the first gas introduced and then followed by ethylene and the make up gas which usually was helium. It was thought that by adding hydrogen first, the surface would be passivated and ethylene decomposition would not occur. Another possible explanation could be that the CO in the gas line as well as a major contaminant in the gas bottles was blocking sites on the surface if ethylene was introduced first. To resolve this question, one must follow both the poison as well as the reaction intermediate at the same time.

In this chapter, 2-IR 1-visible sum frequency generation will be used to investigate the coadsorption systems of CO and ethylene and CO and propylene at high pressures and room temperature as well as the poisoning of ethylene hydrogenation by CO. 2-IR 1-visible sum frequency generation is ideal for these experiments because with two input infrared beams, two spectral region can be observed at the same time. This setup will allow for the simultaneous detection of CO as well as the ethylene reaction intermediate.

A diagram of the 2-IR 1-visible SFG geometry is shown in figure 6.1. Under this setup, two optical parametric systems have to operate simultaneously in addition to generating the visible beam used in the experiment. In these, all three beams have to be overlapped on the surface spatially as well as temporally. The latter restriction is especially difficult since one of the infrared had to be delayed in time with respect to the other. This was eventually accomplished by extending the path of the pump beam in the $LiNbO_3$ OPG/OPA to match the AGS beam. This was done rather than delaying the infrared after generation to prevent

loss in energy. The two spectral regions investigated are at 1800 to 2200 cm^{-1} for CO and 2700 to 3100 the olefin species.

A. CO ethylene coadsorption

Starting in UHV a Pt(111) crystal was cleaned by cycles of 12 minute argon sputtering ($3x10^{-5}$ torr Ar pressure, 1000 volts, and 20 mA emission current) and heating in oxygen (5x10-7 torr O_2, 1123K). As the last step of the cleaning cycle following the oxygen treatment, the sample was annealed for 2 minutes at $2x10^{-9}$ torr and 1133K to form a clean and well-ordered surface. Auger electron spectroscopy was used to check the sample cleanliness. During cooling to room temperature, 5L exposure of ethylene was followed by 5L exposure of CO at 338K and 298K respectively. In figure 6.2A, the CO speak is shifted to 2005 cm^{-1} from the normal atop terrace site at 2095 cm^{-1}. The ethylene adsorbs as ethyledyne on the surface with its vibrational peak at 2880 cm^{-1}. In figure 6.2B, the CO pressure was increased to $1x10^{-7}$ torr at 298K without changing anything else. An increase in the CO intensity is observed without any shifting in the vibrational frequency. The ethylene spectrum remains unchanged with the increased CO pressure. Figure 6.2C shows the CO pressure increased to 100 torr at 298K. The CO spectrum shifts to 2030 cm^{-1} but is still unable to completely displace the ethylene from the surface.

Closer examination of the coadsorption system in figure 6.3 shows that two CO peaks appear after the pressure is increased. The surface is first predosed

with 10L of ethylene at 300K to form ethylidyne. Afterwards the CO was introduced at various pressures. In this coadsorption environment, the CO frequency red shifts by approximately 80 wavenumbers as a result of the CO coverage effects and its interaction with the resulting ethylidine and hydrogen. Most notably is the appearance of two CO peaks at higher CO pressures, indicating the presence of CO at different surface environments To check for the role of hydrogen on the surface, figure 6.4 shows the result of ethylene dosed onto the surface at 400K, above the desorption temperature of the remaining hydrogen. The absence of the two CO peaks indicates that the hydrogen was responsible for this effect. This was further checked by dosing the ethylene at 300K to form ethylidyne and then increase the temperature to 400K to drive off the hydrogen. Results from this experiment, shown in figure 6.5, is comparable to that of ethylene dosed at 400K. To observe the behavior of the CO ethylene coadsorbed system where the ethylene pressure dominates, figure 6.6 shows that even at high ethylene pressures of 40 torr, CO dosed at 10^{-7} torr prior to the ethylene still remains.

B. CO propylene coadsorption

Starting in UHV a Pt(111) crystal was cleaned by cycles of 12 minute argon sputtering ($3x10^{-5}$ torr Ar pressure, 1000 volts, and 20 mA emission current) and heating in oxygen (5x10-7 torr O_2, 1123K). As the last step of the

cleaning cycle following the oxygen treatment, the sample was annealed for 2 minutes at $2x10^{-9}$ torr and 1133K to form a clean and well-ordered surface. Auger electron spectroscopy was used to check the sample cleanliness. Auger electron spectroscopy was used to check the sample cleanliness. During cooling to room temperature, 5L exposure of propylene was followed by 5L exposure of CO at 338K and 298K respectively. At room temperature, the CO pressure was increased and both the propylene and CO species were followed. In figure 6.7, the C-H stretch region of propylene is shown. Starting with the propylidyne species, three prominent peaks are shown. The high frequency peat at 2960 cm^{-1} was assigned to the asymmetric CH_3 stretch of the terminal group while the 2920 cm^{-1} species is assigned to the symmetric CH_3 stretch and the small feature at 2855 cm^{-1} is assigned to Fermi resonance by Cremer et, al. As the CO pressure is increased, the high energy asymmetric CH_3 peak drops in intensity while the symmetric CH_3 peak increases. This effected is attributed to tilting of the propylidyne species. At CO pressures above a torr, the propylidyne signal disappears leading one to suspect either dissociation or desorption. Figure 6.8 shows the corresponding CO spectrum at the same conditions. On the CO side, little change in the spectrum is seen until propylene is no longer on the surface. At 1 torr and above, the CO spectrum shifts to high frequency along with signal intensity increases. This seems to indicate that the propylene did not dissociate on the surface but rather desorbed.

C. CO poisoning of ethylene hydrogenation

Starting in UHV a Pt(111) crystal was cleaned by cycles of 12 minute argon sputtering ($3x10^{-5}$ torr Ar pressure, 1000 volts, and 20 mA emission current) and heating in oxygen (5x10-7 torr O_2, 1123K). As the last step of the cleaning cycle following the oxygen treatment, the sample was annealed for 2 minutes at $2x10^{-9}$ torr and 1133K to form a clean and well-ordered surface. Auger electron spectroscopy was used to check the sample cleanliness. During cooling to room temperature, CO was leaked in to cover the surface. One torr of CO was then added followed by 10 torr ethylene, 100 torr hydrogen and the total pressure was made up to atmosphere pressure by helium.

Figure 6.9 shows the percent ethane produced at various temperatures and the corresponding SFG spectra. The gas phase characterization of reactants and products were done through a gas chromatograph operating in FID mode. Figure 6.9 shows that at room temperature CO occupies the terrace sites and the in the olefin region, the appearance of a broad C-H peak. At this point, little ethane is detected. At 373K, CO still occupy the surface and the same C-H signature. At this point, ethylene hydrogenation on a clean Pt(111) surface would show tremendous turnover however, CO is still blocking sites necessary for ethylene hydrogenation. At 425K, CO desorbs off the surface and ethylene hydrogenation proceeds and in the C-H region, the reaction intermediate species assigned to π-bonded ethylene are seen. After the reaction consumes all of the reactants, and

the crystal returns to room temperature, CO returns to it atop site and the C-H signature present before is gone.

To further study the affect of CO contamination , the CO pressure was increased to 3 torr with other reactants held at previous conditions. In this experiment, the surface was predosed with 10^{-7} torr CO and then high pressure hydrogen was added. The SFG result is shown in figure 6.10 where the CO is completely removed with the addition of high pressure hydrogen. At higher CO pressures of 3 torr CO readsorbs on the Pt(111) surface as seen in figure 6.11. With increase temperature, the spectra first blue shifts to account for the increased coverage due to hydrogen desorption. Then above the CO desorption temperature, the SFG intensity drops and the peak frequency red shifts for reasons described in the high pressure CO experiments. At the respective temperatures, the gas phase composition was analyzed and the turn over rates are plotted in figure 6.12. In figure 6.13, it is clearly shown that the ethylene hydrogenation reaction rate stays relatively flat until the CO desorption temperature is reached. The left side of the graph shows the turn over rate measured in this experiment and this is compared to the rate without CO as published by Zaera et. al. In figure 6.14 the turnover rate for various CO coverage is shown. This plot show that with very low coverage of CO the surface can be protected from contaminates and readily removed by high pressure hydrogen. If leaks to the atmosphere occur, contaminates drastically affect the reaction.

CO poisons the hydrogenation of ethylene by blocking sites. Since CO is a major component of background gasses its role as a poison is always present in high pressure reactions. If olefin hydrogenation reactions are to be studied, it is important that CO contamination be well controlled and to avoid possible conflicts, reactions should be studies at above 450K to desorb CO from the surface.

References

1. B. Bent, Ph.D. Thesis, University of California Berkeley, (1986)
2. X. Su, P.C. Cremer, Y.R. Shen, G.A. Somorjai, Phys. Rev. Lett., **77**, 3858, (1996).
3. P.C. Cremer, X. Su, Y.R. Shen, G.A. Somorjai, J. Phys. Chem., **100,** 16302, (1996).
4. A. Bandara, S. Dobashi, J. Kubota, K. Onda, A. Wada, K. Domen, C. Hirose, S.S. Kano, Surf. Sci., **387**, 312, (1997).
5. C. Klunker, M. Balden, S. Lehwald, W. Daum, Surf. Sci., **360,** 104, (1996).
6. H. Harle, K. Mendel, U. Metka, H.R. Volpp, L. Willms, J. Wolfrum, Chem. Phys. Lett., **279**, 275, (1997).
7. F. Zaera, JACS, 111, 4240 (1989)

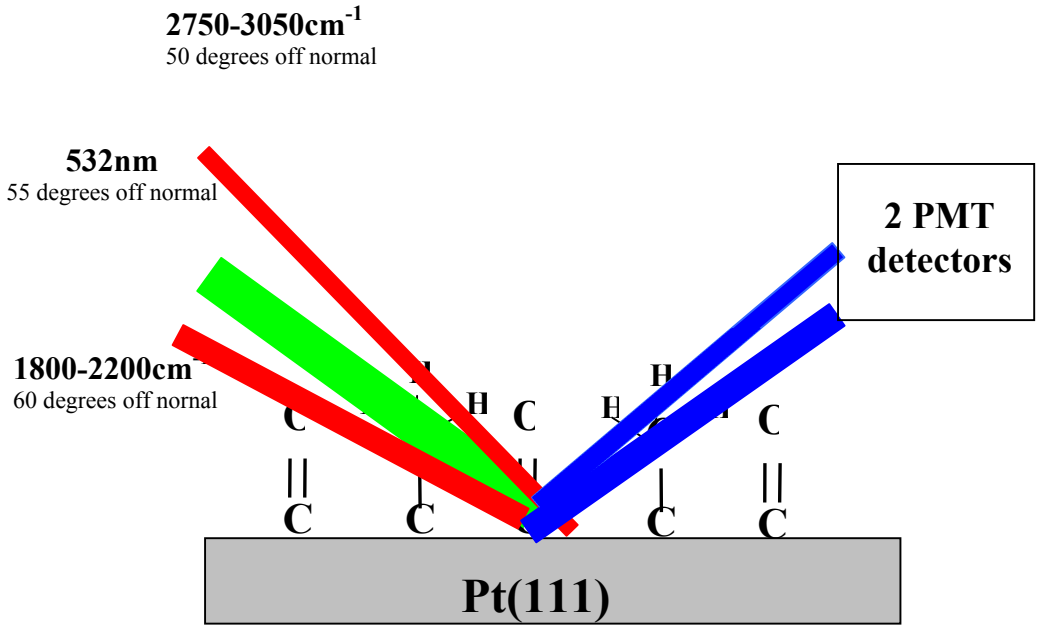

Figure 6.1 Setup for 2-IR 1-visible SFG experiments.

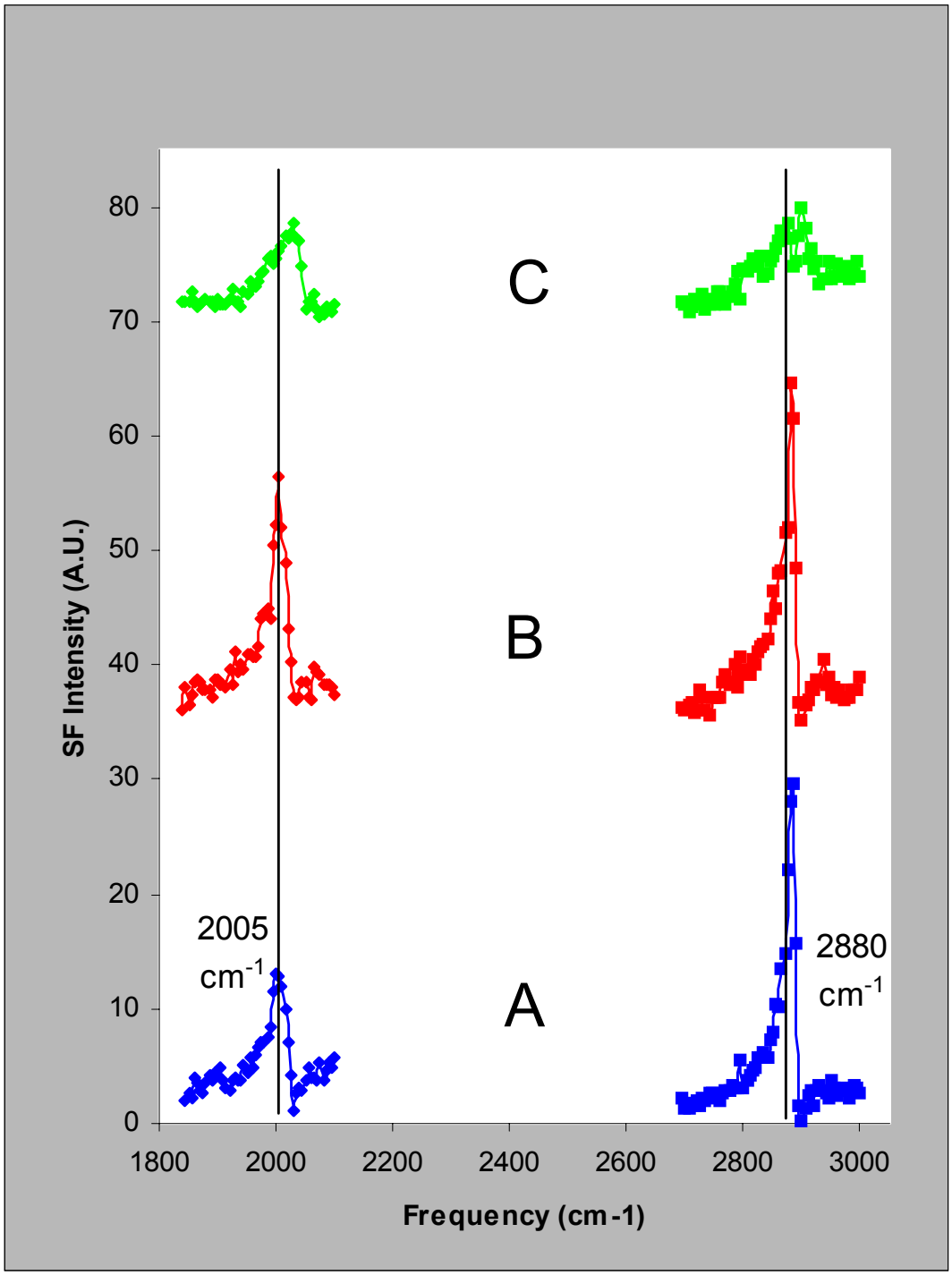

Figure 6.2 CO ethylene coadsorption

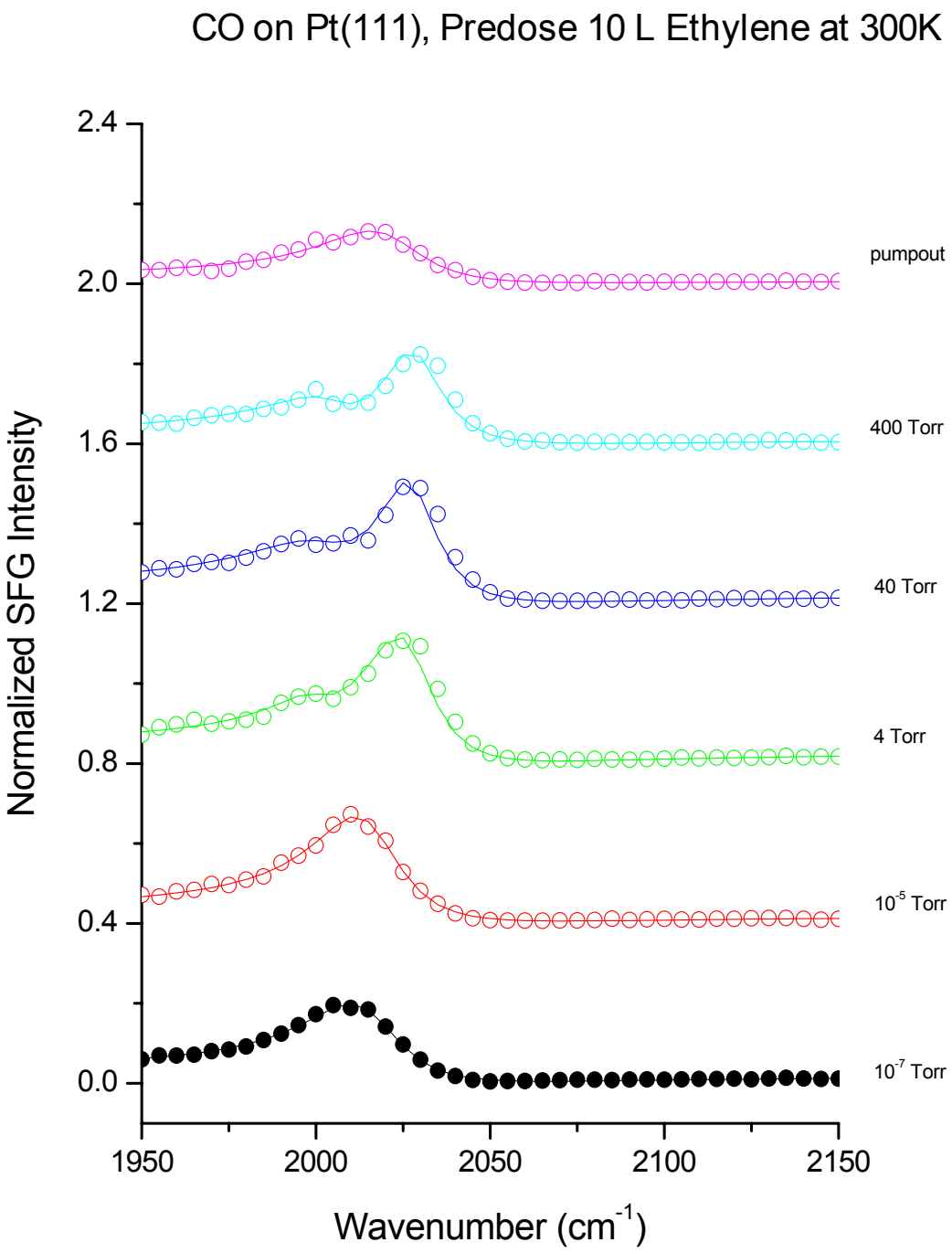

Figure 6.3 After 10L of ethylene at 300K, CO pressure is increased. Two CO peaks appear indicating that CO occupy defect sits at low pressures and terrace site are occupied at high CO pressure.

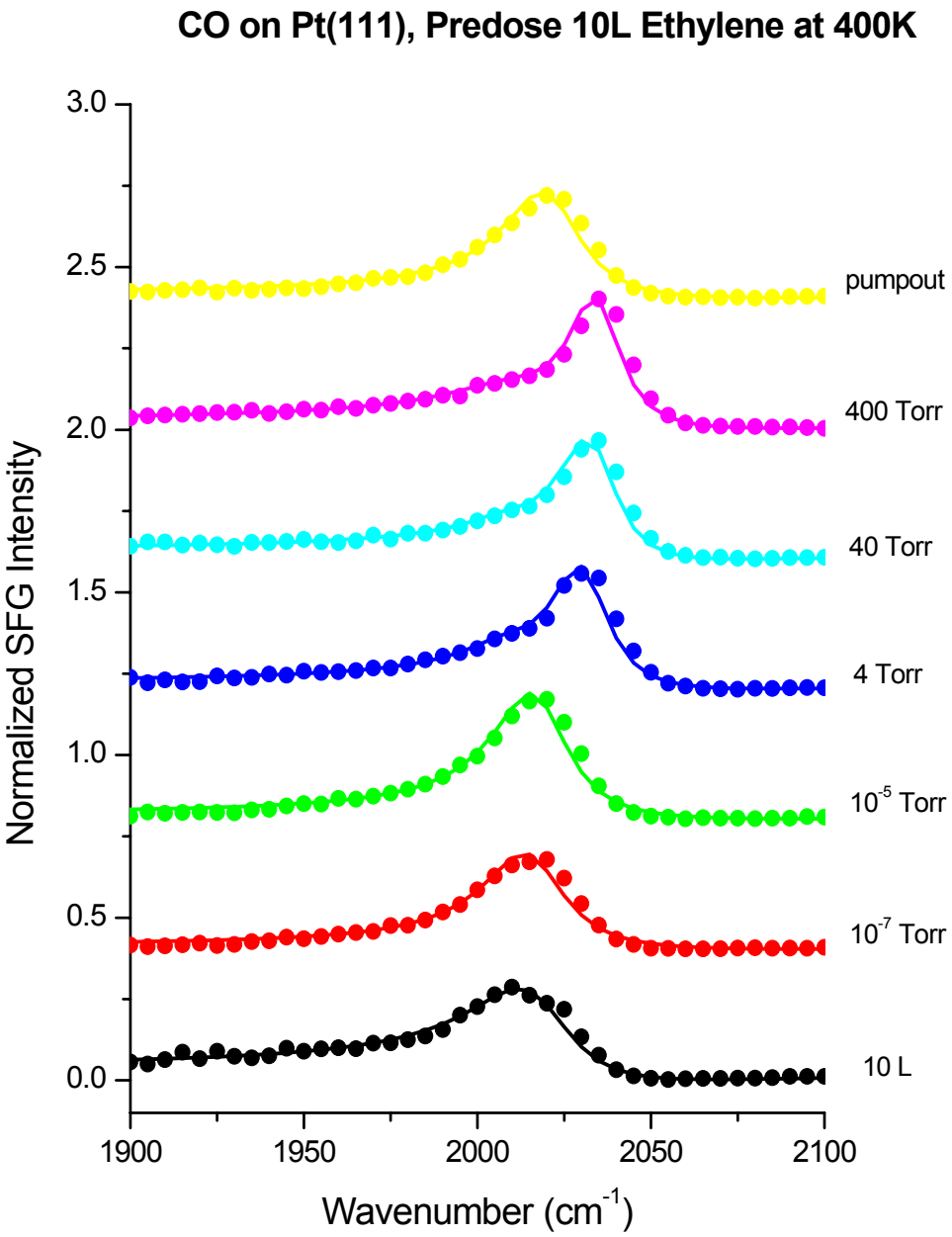

Figure 6.4 After 10L of ethylene at 400K, CO pressure is increased. The absence of two CO peaks at high pressure resulted from the desorption of hydrogen from the surface.

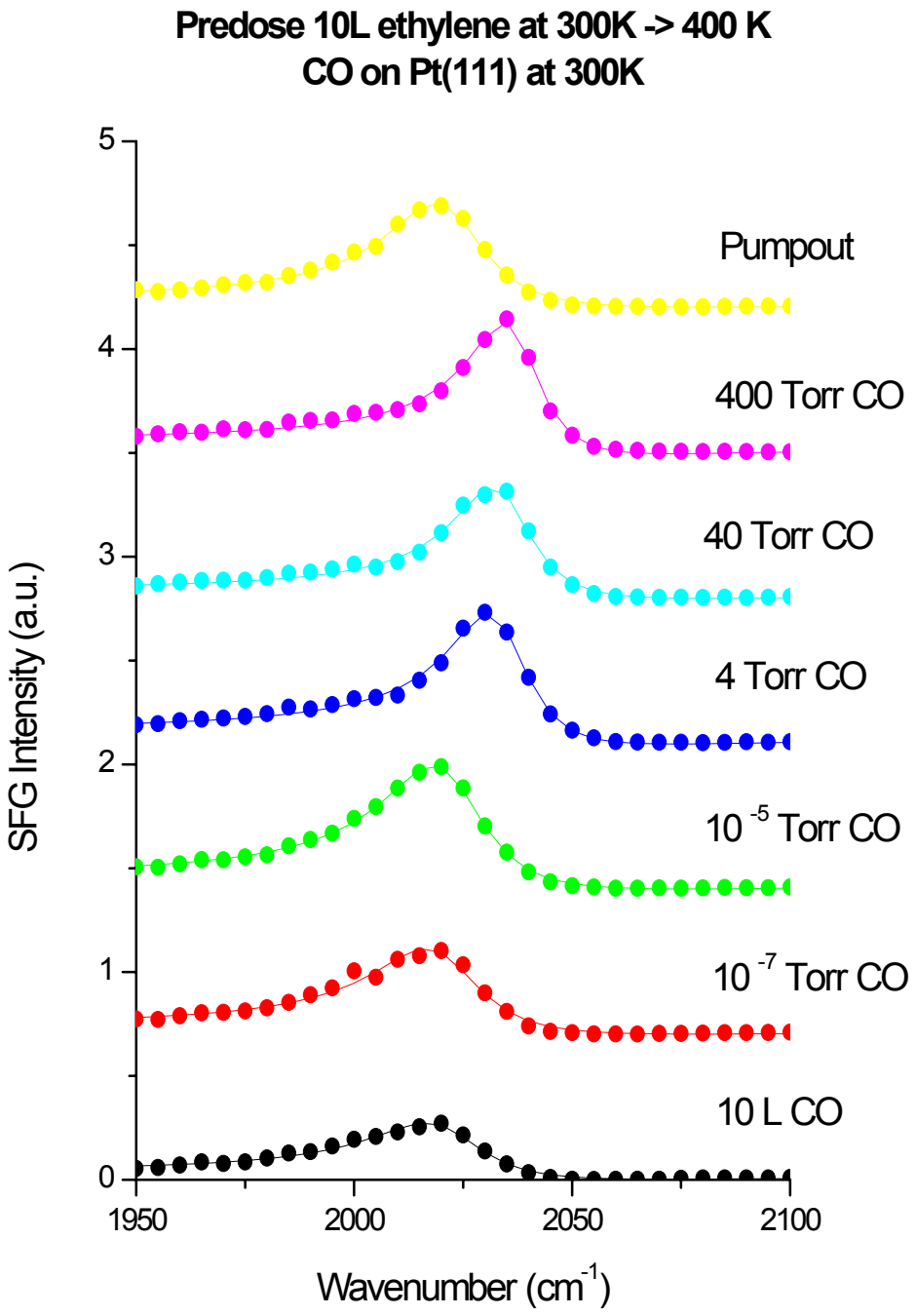

Figure 6.5 After 10L of ethylene at 300K, the surface was heated to 400K to desorb off hydrogen and then cooled back to 300K where CO pressure is increased.

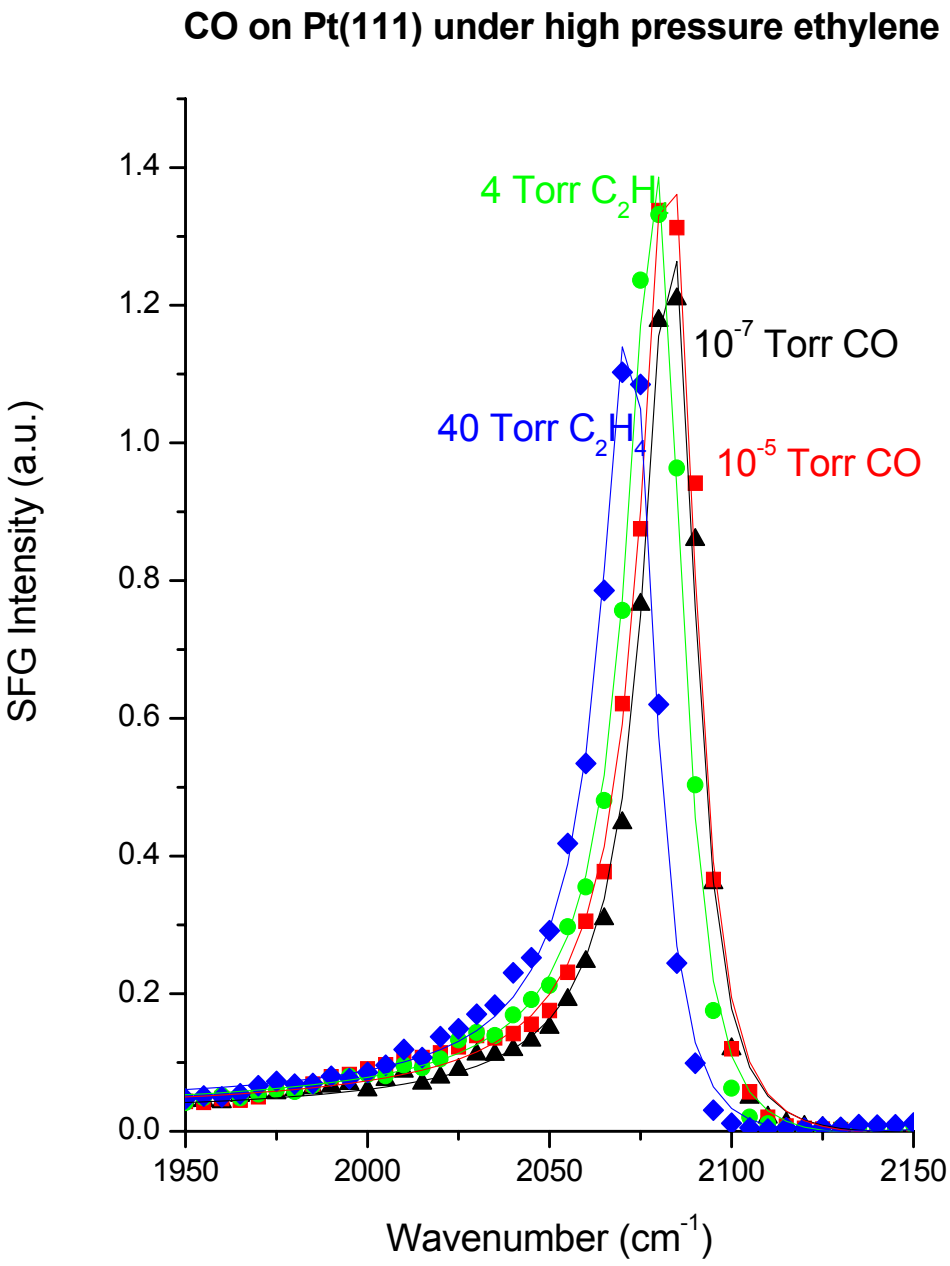

Figure 6.6 After 10^{-7} torr CO pressure at 300K, ethylene pressure is increased.

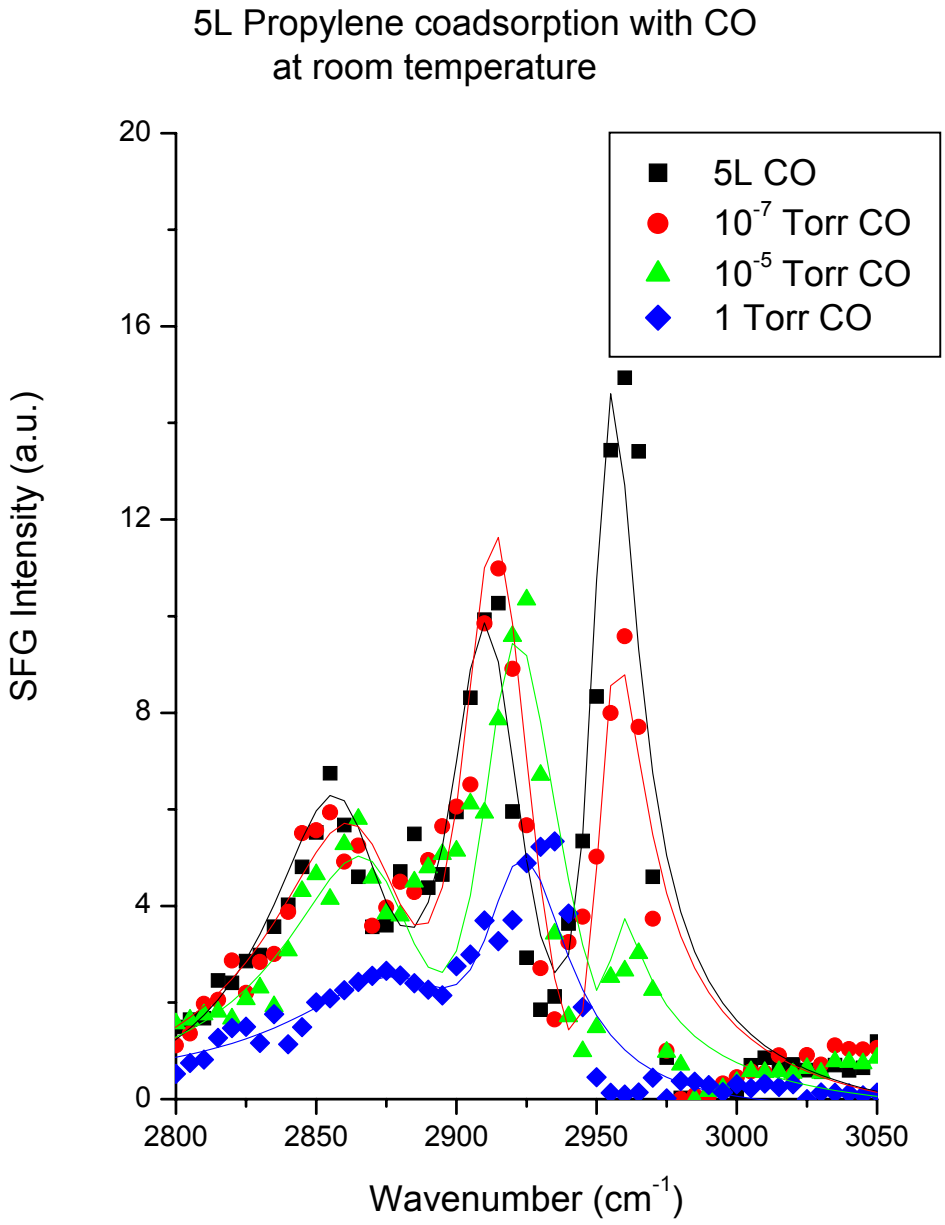

Figure 6.7 CO pressure effects on propylidyne. At higher CO pressures, propylidyne undergoes conformation changes.

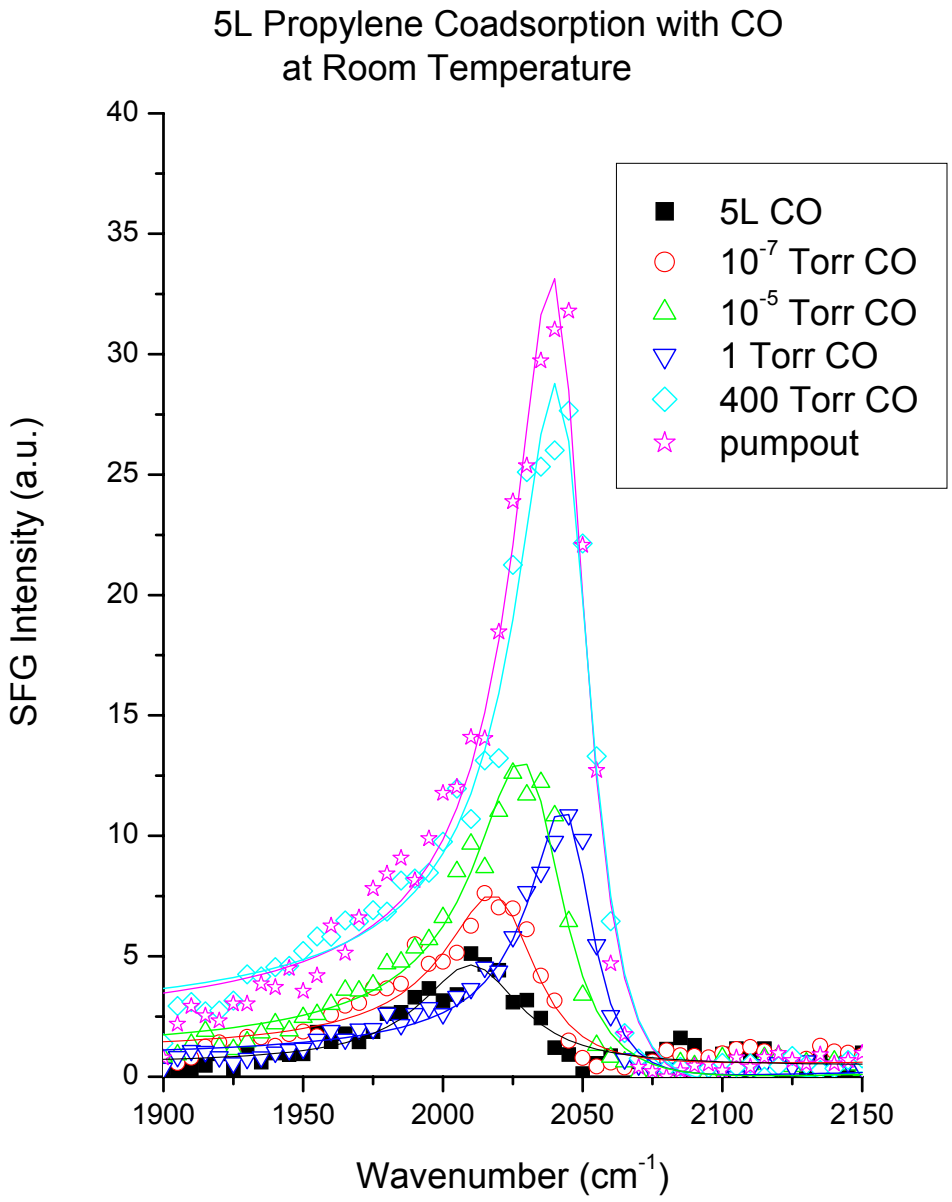

Figure 6.8 CO spectrum in CO propylene coadsorption as CO pressure is increased after coadsorbing with 5L propylene.

figure 6.9

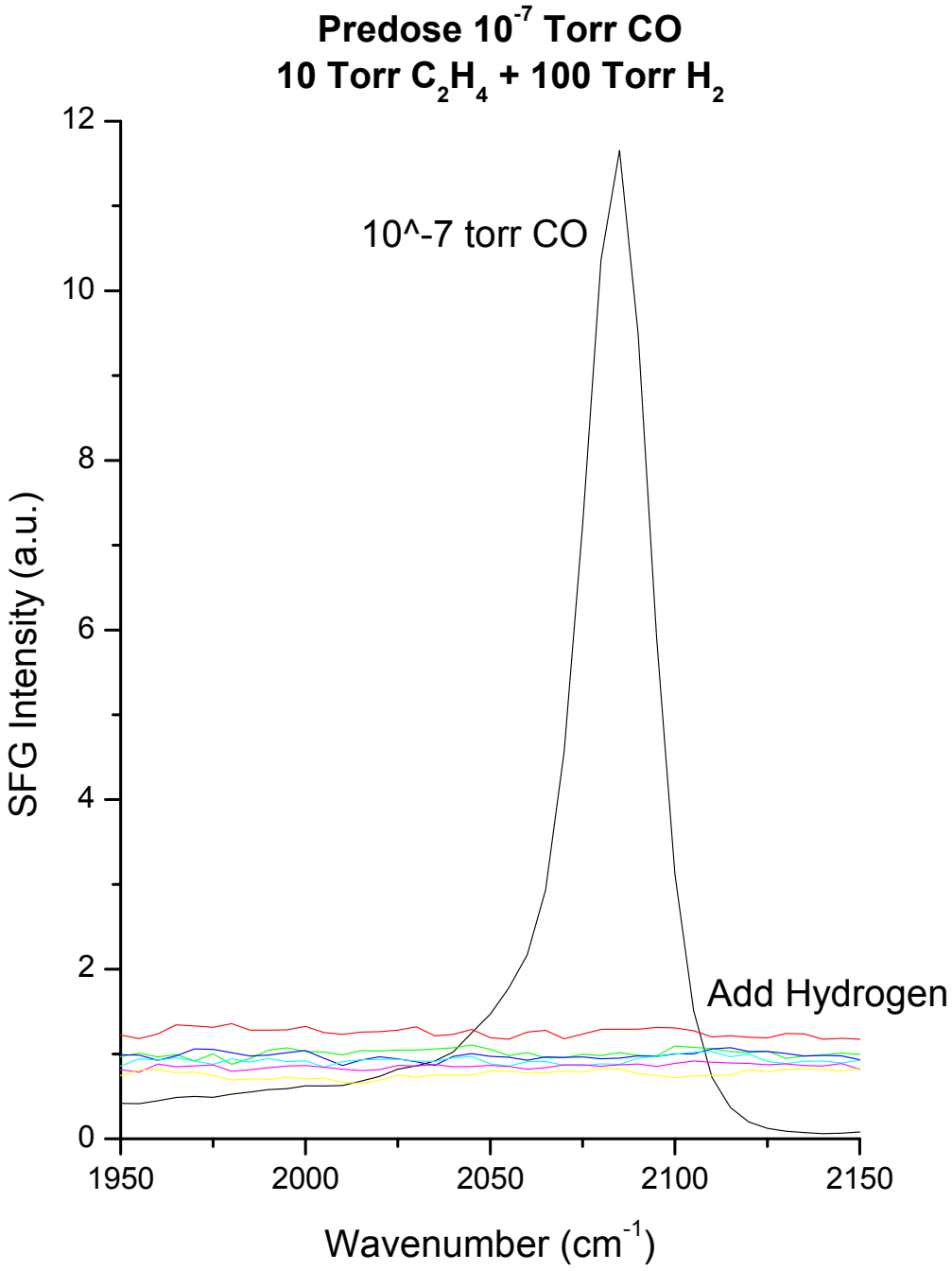

Figure 6.10 SFG spectra of high pressure hydrogen effects on CO adsorption.

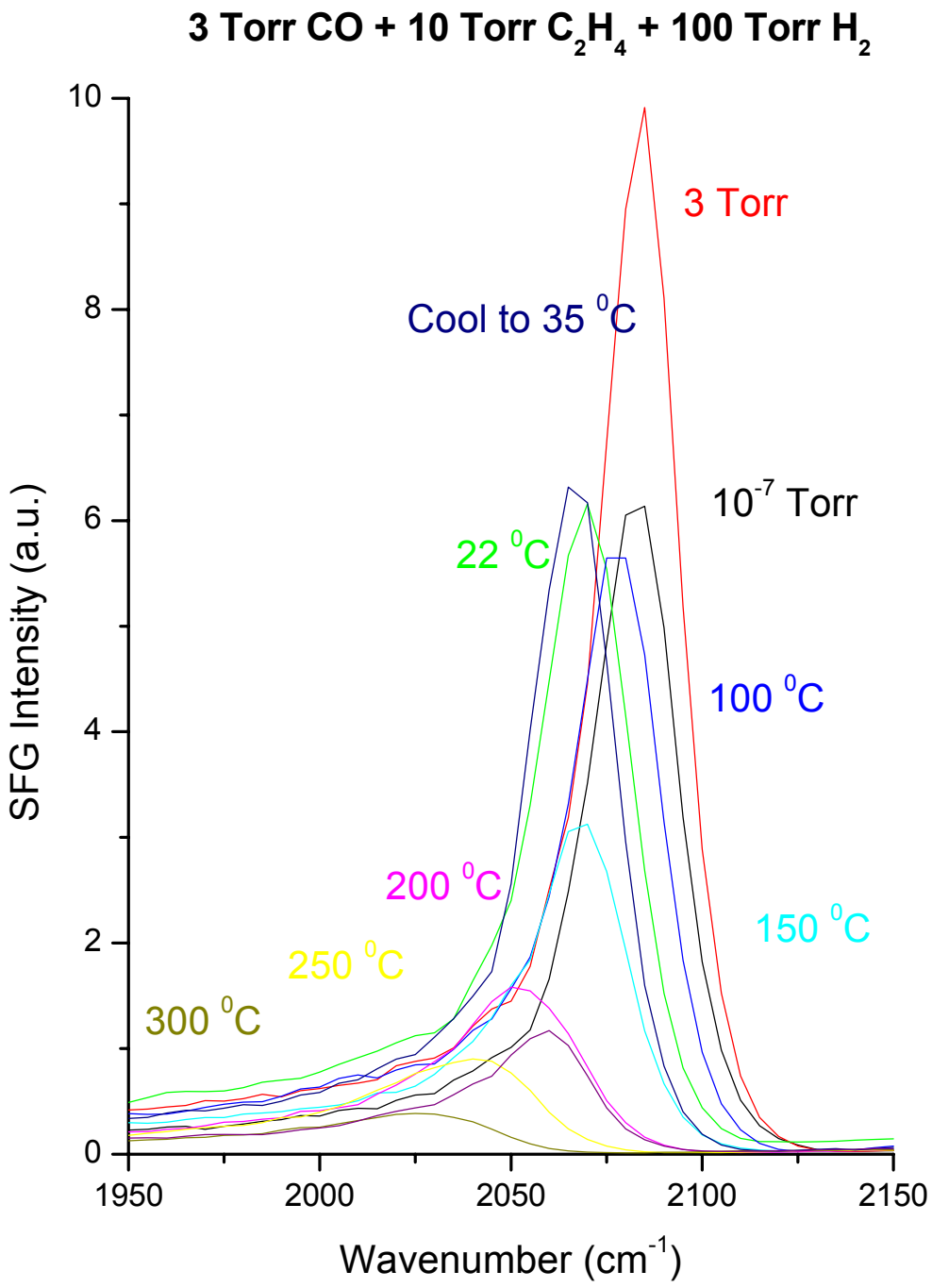

Figure 6.11 SFG spectra of 3 torr CO at ethylene hydrogenation reaction condition at various temperatures.

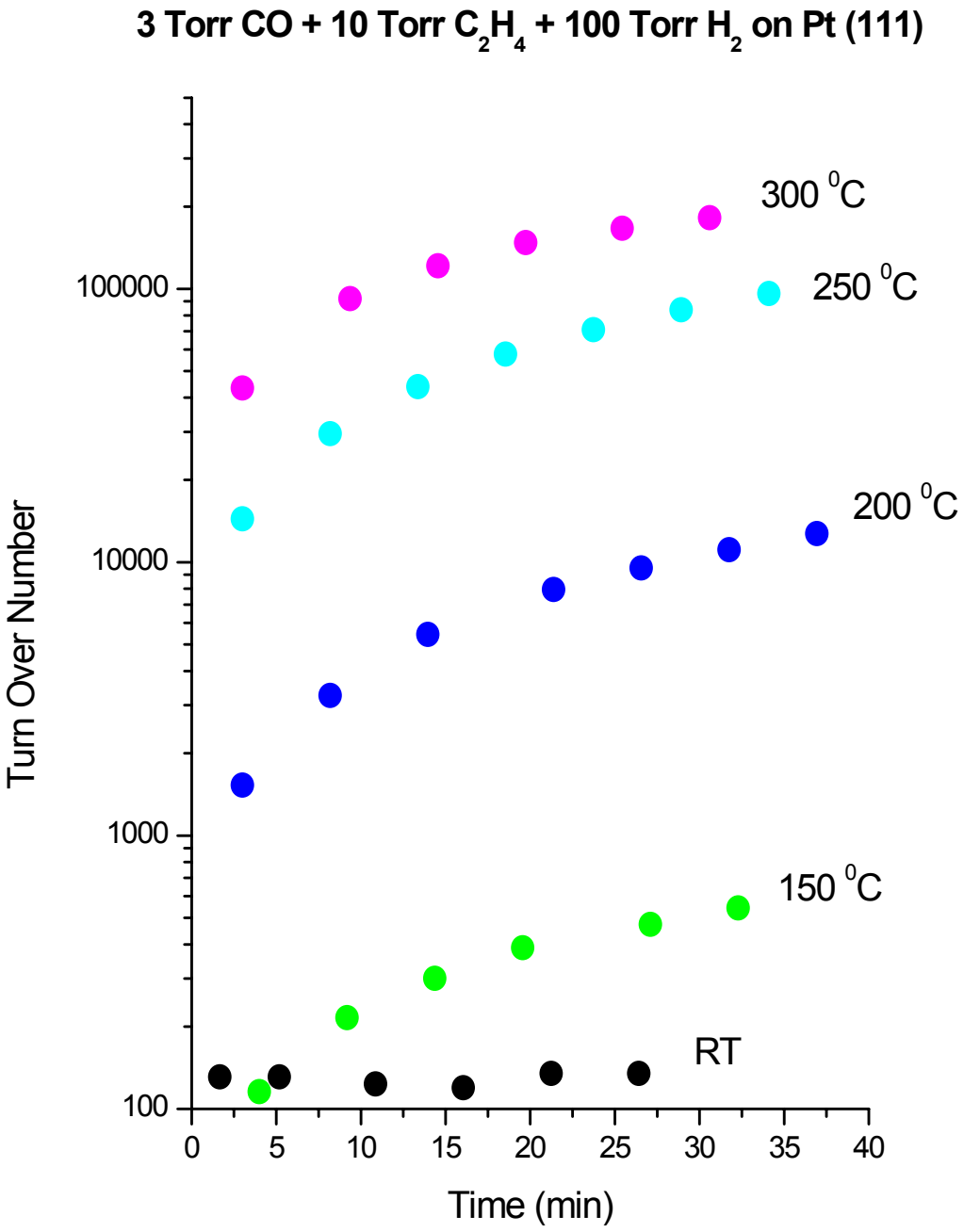

Figure 6.12 Turnover rates of ethylene hydrogenation reaction condition at various temperatures with CO contamination.

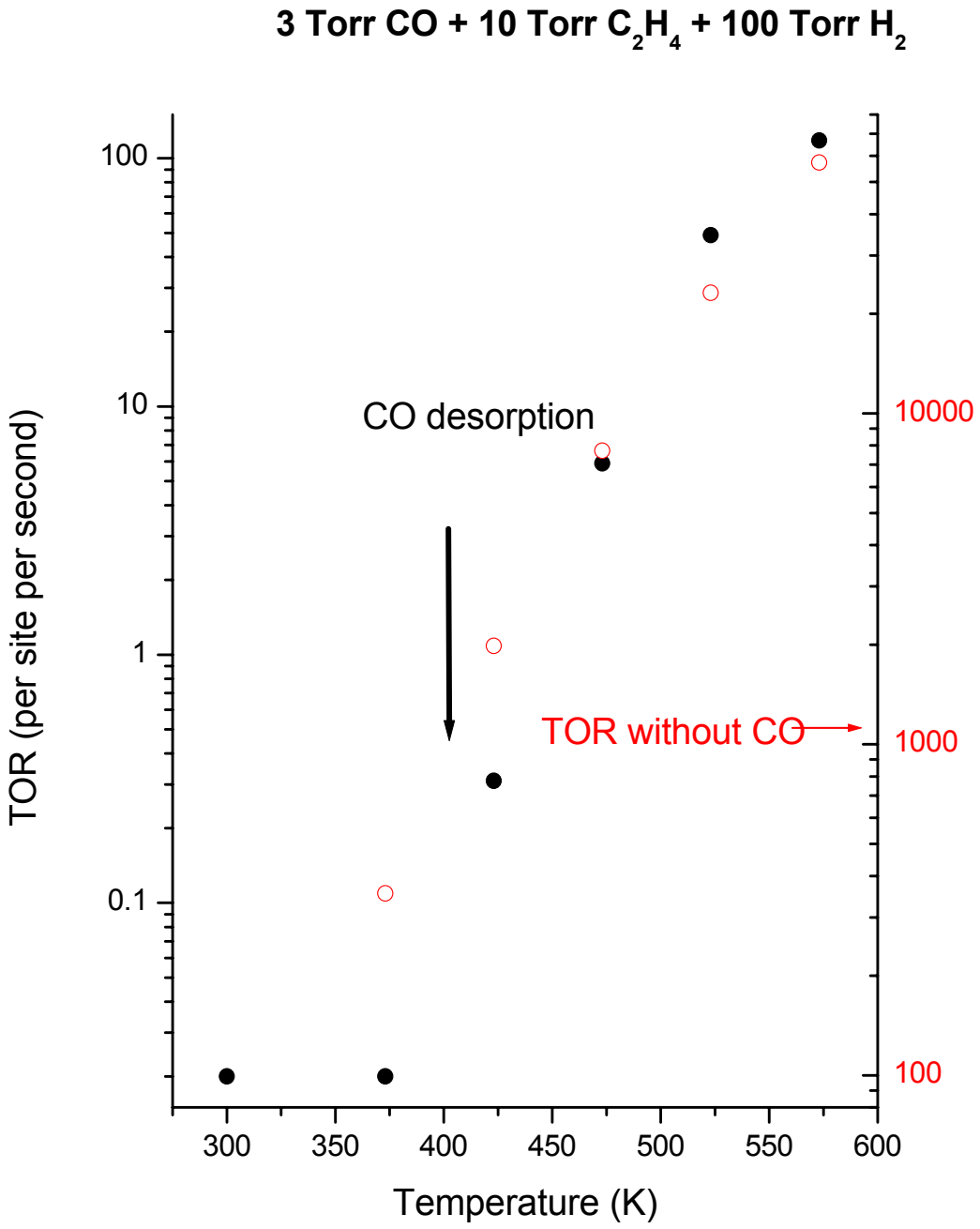

Figure 6.13 Comparing the turnover rate with and without CO contamination. Below the CO desorption temperature CO poisons the reaction.

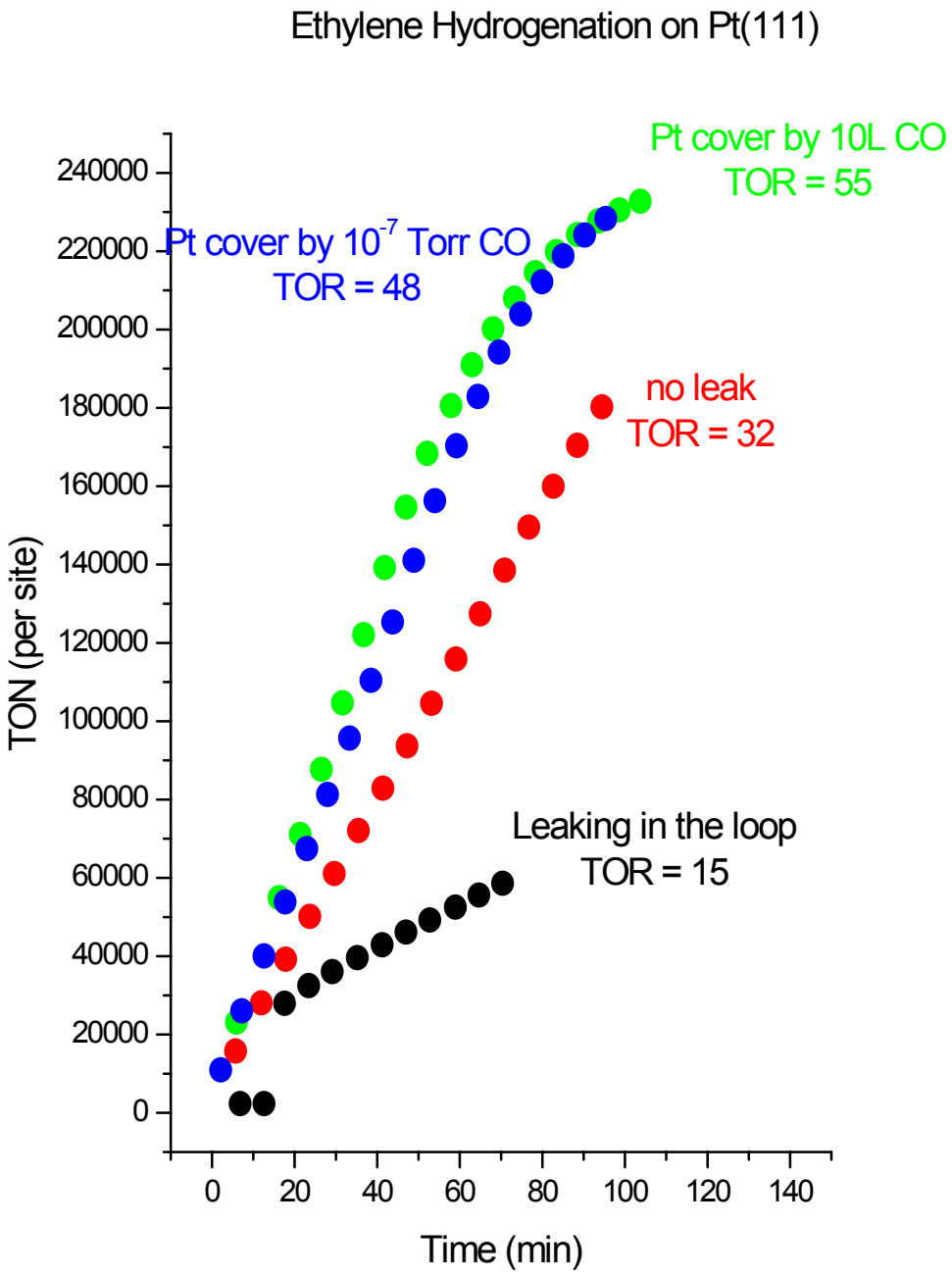

Figure 6.14 . Ethylene hydrogenation turnover rates for various CO coverage.

Appendix

A. Laser System Parts List

1)	R_{max} 1064nm 45° P	(CVI Y1-1025-45-P)
2)	R 20% 1064nm 45° P	(CVI BS1-1064-20-1025-45P)
3)	R_{max} 1064nm 45° P	(CVI Y1-1025-45-P)
4)	R_{max} 1064nm 45° P	(CVI Y1-1025-45-P)
5)	20cm fl, ar/ar 1064nm	(CVI PLCX-25.4-103.0-C-1064)
6)	-15cm fl, ar/ar 1064nm	(CVI PLCC-25.4-77.3-C-1064)
7)	R_{max} 1064nm 45° P	(CVI Y1-1025-45-P)
8)	R_{max} 1064nm 45° P	(CVI Y1-1025-45-P)
9)	R_{max} 1064nm 45° P	(CVI Y1-1025-45-P)
10)	R_{max} 1064nm 45° P	(CVI Y1-1025-45-P)
11)	LWP 45° P R1064nm P-Pol T1300nm S-Pol	(CVI LWP-45-RP1064-TS1300-PW-1025C)
12)	R 60% 1064nm 45° P	(CVI BS1-1064-60-1025-45P)
13)	Quarter Waveplate 1064nm multiple order	
14)	Telescope, slightly divergent	
15)	Telescope, slightly divergent	
16)	LBO crystal	(Casix, LBO 8x8x7mm, x-cut, ar/ar)
17)	Pellin Broca prism uncoated	(CVI PLBC-10.0-79.5-C)
18)	R_{max} 1064nm 45° P	(CVI Y1-1025-45-P)
19)	R 20% 532nm 45° P	(CVI BS1-532-20-1025-45P)
20)	R_{max} 1300nm T_{max} 532nm 45° P	(CVI SWP-45-RS1300-TP532-PW-1025-P)
21)	BBO crystal	(Casix, BBO 5x5x10mm, ϕ=0° θ=22.47° polished)
22)	BBO crystal	
23)	R_{max} 1300nm T_{max} 900nm 45° P	(CVI LWP-45-RP532-TS900-PW-1025-C)
24)	Pellin Broca prism uncoated	(CVI PLBC-10.0-79.5-C)
25)	Telescope, slightly divergent	
26)	Telescope, slightly divergent	
27)	R_{max} 532nm 0°	(CVI Y2-1025-0)
28)	Prism ar 532nm	(CVI PG-SQM-1037-C)
29)	PLCX 5cm 700-1000 nm ar	(CVI PLCX-25.4-25.8-C-700-1000-0)
30)	PLCX 50cm 700-1000 nm ar	(CVI PLCX-50.8-257.5-C-700-1000-0)
31)	1200 line grating 1000nm blaze	(CVI grating, 1200 line, 1000nm 30x30mm)

32) Silicon plate at Brewster angle
33) AGS crystal (Cleveland crystals, $AgGaS_2$ 9x11x16.5mm)
34) Ge plate at Brewster angle (CVI Ge, 5.5mic, 20mmx3"x1.5mm uncoated)
35) R_{max} 1064nm 45° P (CVI Y1-1025-45-P)
36) R 20% 1064nm 45° P (CVI BS1-1064-20-1025-45P)
37) R_{max} 1064nm 45° P (CVI Y1-1025-45-P)
38) R_{max} 1064nm 45° P (CVI Y1-1025-45-P)
39) R_{max} 1064nm 45° P (CVI Y1-1025-45-P)
40) PLCC -10cm 1064nm ar/ar (CVI PLCC-25.4-51.5-C-1064)
41) PLCX 25cm 1064nm ar/ar (CVI PLCX-25.4-128.8-C-1064)
42) PLCX 15cm 1064nm ar/ar (CVI PLCX-50.8-77.3-C-1064)
43) PLCC –7.5cm 1064nm ar/ar (CVI PLCC-25.4-36.8-C-1064)
44) R_{max} 1064nm T_{max} 1500nm 45° P (CVI LWP-45-R1064-T1500-PW-1025-UV)
45) $LiNbO_3$ crystal (Casix, 11x11x50mm, ϕ=-90° θ=47°, ar/ar 1064nm)
46) Copper mirror (Spawr Ind., 1"dia., ICU-001-Flat)
47) R_{max} 1064nm T_{max} 1500nm 45° P (CVI LWP-45-R1064-T1500-PW-1025-UV)
48) $LiNbO_3$ crystal (Casix, 11x11x50mm, ϕ=-90° θ=47°, ar/ar 1064nm)
49) R 1064 T 3.5um 0° sapphire (CVI OPOM-0-R1064-T2500-4000-PW-1012)
50) Ge plate at Brewster angle (CVI Ge, 5.5mic, 20mmx3"x1.5mm uncoated)
51) PLCC -10cm
52) PLCX +20cm

B. Distances between optical components

The distances between the optical components are approximated from the center of the optic of the nearest face except when noted otherwise. This distinction is necessary because in many instances the optics are angled to each other.

For the AGS system:

Laser to #1	7.5cm	
#1 to #2	4.0cm	
#2 to #3	4.5cm	
#3 to #4	16.5cm	
#4 to #5	6.5cm	
#5 to #6	4.0cm	
#6 to #7	68.5cm	
#7 to #8	31.0cm	
#8 to #9	164.0cm	
#9 to #10	5.5cm	
#10 to #11	138.5cm	
#2 to #12	6.0cm	
#12 to #13	15.5cm	
#13 to #14	5.5cm	
#14 to #15	1.5cm	
#15 to #16	10.5cm	center of the LBO crystal
#16 to #17	14.0cm	center of the LBO crystal
#17 to #18	32.0cm	
#18 to #19	4.5cm	
#19 to #20	8.0cm	
#20 to #21	12.0cm	
#21 to #22	18.5cm	
#22 to #23	15.0cm	
#23 to #24	20.0cm	
#24 to #25	8.0cm	
#25 to #26	3.5cm	
#26 to #27	55cm	
#23 to #28	6.0cm	
#28 to #29	9.0cm	

#29 to #30	53.0cm
#30 to #31	19.0cm
#20 to #32	6.0cm
#32 to #51	10.5cm
#51 to #52	8.0cm
#52 to #11	22.5cm
#11 to #33	23.5cm
#33 to #34	11.0cm

For the $LiNbO_3$ system:

#12 to #35	25.0cm
#35 to #36	50.0cm
#36 to #37	86.0cm
#37 to #38	5.5cm
#38 to #39	102.5cm
#36 to #41	8.0cm
#41 to #43	18.0cm
#39 to #40	not currently in use
#40 to #42	not currently in use
#39 to #47	28.0cm
#44 to #45	74.0cm
#45 to #46	4.0cm
#44 to #47	11.0cm
#47 to #48	19.5cm
#48 to #49	5.0cm
#49 to #50	16.0cm